Journal of Magnetism and Magnetic Materials 323 (2011) 2592–2607

Contents lists available at ScienceDirect

Journal of Magnetism and Magnetic Materials

journal homepage: www.elsevier.com/locate/jmmm

Magnetic phase diagrams of the CrB- and FeB-type HoSi compounds

P. Schobinger-Papamantellos [a,*], K.H.J. Buschow [b], J. Rodríguez-Carvajal [c]

[a] Laboratory of Crystallography, ETH-Zurich, 8093 Zürich, Switzerland
[b] Van der Waals-Zeeman Institute, University of Amsterdam, NL-1018 XE, The Netherlands
[c] Institut Laue-Langevin, 156X, 38042 Grenoble Cédex, France

ARTICLE INFO

Article history:
Received 10 May 2011
Available online 6 June 2011

Keywords:
Long period magnetic structure
Incommensurate magnetic structure
Neutron diffraction
Holmium silicon alloy

ABSTRACT

The temperature magnetic phase diagrams of the dimorphic HoSi compound were studied by neutron diffraction. The sample comprises 35.5% CrB- (*Cmcm*) and 64.5% FeB-type (*Pnma*) of structure. Both phases order antiferromagnetically below $T_N=25$ K and undergo first-order magnetic transitions at $T_{ic}=16.5$ K. Their T-phase diagrams comprise a low temperature (*LT*) 2.7 K$-T_{ic}$ and a high temperature (*HT*) range $T_{ic}-T_N$ with distinct wave vectors.

The *LT* magnetic ordering of the CrB-type HoSi with the wave vector $\boldsymbol{q}_1=(1/2, 0, 1/2)$ corresponds to a uniaxial magnetic structure, with the Ho moments along the shortest axis *c*. At 2.7 K the ordered moment value is 8.6(2) μ_B/Ho atom. The *HT* ordering, described by the wave vector $\boldsymbol{q}_2=(q_{2x}, 0, q_{2z})$ with a T-variable length, corresponds to an amplitude modulated structure.

The magnetic ordering of the FeB-type HoSi requires two symmetry independent vectors $\boldsymbol{q}_3=(0, q_{3y}, q_{3z})$ for the *LT*- and $\boldsymbol{q}_4=(q_{4x}, q_{4y}, 0)$ for the *HT* range. Both vectors correspond to sine wave modulated structures with the Ho magnetic moments confined along the shortest axis *b*. The $\boldsymbol{q}_3$ vector has an almost invariable length vs. *T* close to $\approx(0, 9/17, 1/11)$. At 2.7 K the amplitude of the wave is 10.9(1) μ_B/Ho atom. At T_{ic} $\boldsymbol{q}_3$ jumps to the wave vector $\boldsymbol{q}_4=(q_{4x}, q_{4y}, 0)$ with a T-variable length. At 17 K $\boldsymbol{q}_4=(0.092(1), 0.538(3), 0)$. Around T_{ic} there is a narrow coexistence range of the $\boldsymbol{q}_3$ and $\boldsymbol{q}_4$ competing phases. Various models are discussed and compared with the isomorphic *R*Si (*R*=rare earth) compounds counterparts of HoSi, a comparison that has led us to briefly review the magnetic structures available in the literature for this interesting class of compounds.

1. Introduction

HoSi, like the other *R*Si (*R*=heavy rare-earth) compounds, occurs with two orthorhombic structures [1]: the CrB-type (*Cmcm* Nr. 63, all atoms at 4*c* site: (0, *y*, 1/4)) and the FeB-type (*Pnma* Nr. 62, all atoms at 4*c* site: (*x*, 1/4, *z*)). The compound TmSi is an exception and adopts exclusively the CrB-type. The two structures are related and can be viewed as transposed stacking variables of a common unit; the elongated trigonal rare earth prisms are centred by Si zigzag chains that are stacked so that they share their rectangular sides to infinite prism rows. 3D representations of the two structures will be given in later sections.

Apparently, the rare earth arrangement at the corners of the trigonal prism rows implies competing antiferromagnetic interactions that give rise to geometric frustration effects. For both structure types, these effects lead to the formation of a large variety of long-period commensurate (C) or incommensurate (IC) magnetic structures that can transform into each with changing temperature [2]. More recent results on the *R*Si magnetism not given in the review of reference [2] are discussed below and are summarised in the appendix to facilitate reading.

The CrB-type HoSi compound according to a previous study [3] orders antiferro-magnetically below $T_N=25$ K with a collinear magnetic moment arrangement, with the wave vector $\boldsymbol{q}_1=(1/2, 0, 1/2)$. At 4.2 K the Ho moments ($\mu_{Ho}=7.0$ μ_B) were oriented 12° off the *c*-direction in the plane (*a*, *c*), in agreement with the crystal field calculations [4]. However no further information exists concerning the thermal evolution of this phase. The HoSi sample examined later on by us, in relation to the CrB-type (*T*, *x*) phase diagram [5] of the pseudo-binary system $HoGe_{1-x}Si_x$ (solid solution), was dimorphic (35% CrB- and 64.5% FeB-type) and the high temperature (*HT*) neutron data could not be refined. The reason was the large number of overlapping satellites at higher temperatures as both magnetic structures become incommensurate with the crystal lattice.

It is to be noted that the CrB-type $HoGe_{1-x}Si_x$ (*T*, *x*) magnetic phase diagram [5] for $x>0.2$ comprises (i) a low temperature (*LT*) lock-in phase $\boldsymbol{q}=(1/2, 0, 1/2)$ and (ii) an incommensurate *HT* phase with $\boldsymbol{q}=(q_x, 0, q_z)$ and a first order transition between them at T_{ic}. Contrary, the magnetic structures of CrB-type compounds with $x<0.2$: HoGe and $HoGe_{0.8}Si_{0.2}$ remain incommensurate $\boldsymbol{q}=(q_x, 0, q_z)$ down to 1.2 K. Above T_{ic} the wave vector has a temperature variable

* Corresponding author.
E-mail address: Schobinger@mat.ethz.ch (P. Schobinger-Papamantellos).

0304-8853/$ - see front matter © 2011 Elsevier B.V. All rights reserved.
doi:10.1016/j.jmmm.2011.05.044

length of mainly the q_x component and the Ho magnetic moments order with a pure sinusoidal modulation 5–7° off the shortest axis *c*. T_{ic} and T_N were found to increase linearly with increase in Si concentration (x). Apparently, the *LT* commensurate phase becomes destabilised with decrease in silicon content (x).

Preliminary results [6] on the FeB-type HoSi compound at 8 K suggest a sine wave modulated magnetic structure associated with the incommensurate wave vector $\boldsymbol{q}=(q_x, q_y, q_z)$, which has an almost temperature invariable length in the *LT* range close to $\approx(0, 1/2, 1/11)$. Similar wave vectors were found in isomorphic rare earth *R*Si compounds as mentioned in detail below.

Our T-dependent neutron diffraction study [7,8] on TbSi (T_N=57 K) has shown that the previously reported *LT* commensurate [9] wave vector $\boldsymbol{q}=(0, 1/2, 0)$ remains unchanged between 2 K and T_c and jumps by a first order transition above T_c=36 K to a general reciprocal lattice position $\boldsymbol{q}=(q_x, q_y, q_z)$ with a strongly variable length in a narrow intermediate region 36–40 K and slowing down above 40 K. At 42 K up to T_N the wave vector has again a commensurate $\boldsymbol{q}=(0, 1/2, 1/8)$ value. The CeSi compound has a commensurate wave vector (0, 1/2, 1/16) [10,11] over the entire magnetically ordered regime as found by neutron powder diffraction and μ_{SR} measurements. Our more recent preliminary single crystal neutron data confirmed this wave vector (unpublished results).

Recently the FeB-type DySi compound was found by us to display quite an exotic behaviour [12–14]. At 1.5 K the magnetic ordering requires two wave vectors: a commensurate (0, 1/2, 1/6) and an incommensurate $\boldsymbol{q}=(0, q_y, q_z)$ close to $\approx(0, 1/2, 1/11)$ location with a slightly temperature variable length [12,13]. With increase in temperature the amount of the incommensurate phase increases at the cost of the commensurate phase, which fully disappears above T_{ic}=23.5 K. The wave vector $\boldsymbol{q}=(0, q_y, q_z)$ jumps simultaneously to another location close to $\approx(0, 1/2, 1/7)$ that remains almost unchanged up to $T_N=39\pm1$ K. This quite unusual phenomenon of a single-$\boldsymbol{q}$ *HT* magnetic phase and of a multiple symmetry independent $\boldsymbol{q}$-vectors *LT* phase could be brought into connection with a first order magnetoelastic transition at T_{ic} with a minor monoclinic distortion recently detected by high resolution X-ray diffraction [14]. Apparently the *HT Pnma* orthorhombic DySi structure transforms at T_{ic} to the monoclinic $P2_1/n$ *LT* phase. The two phases have a broad coexistence range below T_{ic}=23.5 K down to 2.7 K where the *HT* phase exists as a metastable phase. Most likely the presence of two slightly different magnetic structures below T_{ic} is related to the structural sample inhomogeneity.

The present study, on one hand, completes the CrB-type $HoGe_{1-x}Si_x$ (T, x) magnetic phase diagram [5] and, on the other hand, provides information on the FeB-type magnetic structure and its thermal behaviour not studied before. It extends the preliminary information on the HoSi FeB-type magnetic ordering reported by us in [6] at 8 K to the entire magnetically ordered regime of the same sample on the basis of neutron diffraction powder data. The results are summarised in a phase diagram and are compared to those of the *R*Si (*R*=rare earth) isomorphic compounds.

2. Experimental and procedures

2.1. Sample preparation

The HoSi sample was prepared by arc melting of the appropriate amount of the elements in an atmosphere of purified argon gas. The purity of the starting materials was 99.9% for holmium and 99.99% for silicon. After arc melting the sample has been vacuum-annealed in a quartz tube for 1 month at 800 °C. Standard X-ray diffraction using CuKα radiation showed that the annealed sample is dimorphic.

2.2. Neutron diffraction

Neutron data were collected on a HoSi powder sample with the DMC multicounter system at the reactor Saphir, Würenlingen (λ=1.703 and 1.709 Å, 2θ: 3–83° and step increment of 0.10°) for a full set of temperatures in the magnetically ordered state in order to derive the T-magnetic phase diagrams. The data analysis is done by the *FullProf Suite* of programs [15]. The structure plots are made by the program FullProf Studio [16] incorporated in [15].

2.3. Paramagnetic state

The refinements of the 26 K HoSi data in the paramagnetic state confirm the sample composition given in [6] with 64.5% FeB-type and 35.5% CrB-type. Results are given in the next sections in Tables 1–4 and Figs. 1 and 2. The obtained low *R*-factors are satisfactory. The refined structural parameters are in fair agreement with more recently obtained room temperature structural parameters based on a precise single crystal X-ray study [17]. The individual calculated profiles of magnetic origin (dotted curves) of the CrB- and FeB-structure types are given in red and blue colours, respectively, below the standard Iobs and

Table 1
Refined structural and magnetic parameters in the paramagnetic and the magnetically ordered state from neutron data of the CrB-type HoSi compound. Space group *Cmcm* (Nr 63), all atoms at sites 4*c*: ±(0, *y*, 1/4). In the range T_{ic}–T_N the wave vector is incommensurate $\boldsymbol{q}=(q_x, 0, q_z)$ with the crystal lattice.

HoSi	CrB-type (*Cmcm*) (35.5%)				
Parameter	26 K	2.7 K	10.9 K	17 K	20 K
a (Å)	4.2159(9)	4.229(1)	4.228(1)	4.227(1)	4.227(1)
b (Å)	10.400(2)	10.426(3)	10.427(3)	10.439(3)	10.429(4)
c (Å)	3.787(1)	3.795(1)	3.793(1)	3.793(1)	3.792(1)
y_{Ho}	0.142(1)	0.138(1)	0.139(1)	0.139(1)	0.142(1)
y_{Si}	0.425(2)	0.431(3)	0.428(2)	0.423(2)	0.424(2)
$\boldsymbol{q}=(q_x, 0, q_z)$	–	$\boldsymbol{q}_1=(1/2, 0, 1/2)$	$\boldsymbol{q}_1=(1/2, 0, 1/2)$	$\boldsymbol{q}_2=(q_x, 0, q_z)$	$\boldsymbol{q}_2=(q_x, 0, q_z)$
q_x, q_z		1/2, 1/2	1/2, 1/2	0.4709(3), 0.5	0.4471(6), 0.5103(6)
$\mu_{oz}(\mu_B)$, φ_c^o	–	8.6(2), 0	8.3(2), 0	9.5(2), 0	8.3(2), −15(2)
R_B%, R_m%	5.2, –	3.4, 3.5	3.7, 3.3	3.0, 3.6	3.2, 5.9
R_{wp}%, R_{exp}%, χ^2	18, 16.3,1.3	10, 4.0, 5.7	10.6, 3.0, 3	10.2, 3.3, 3.5	13.8, 7.0, 3.9

μ_{oz} is the refined wave amplitude (Fourier coefficient) parallel to the *c*-axis or ordered moment value of holmium in the commensurate range for $T\le T_{ic}$=16.5 K. R_B, R_{wp}, R_m% and R_{exp} are the Bragg factor, the reliability factor for the magnetic intensities, the weighted profile intensities, and the expected value related to the statistical accuracy of the data, respectively.

Table 2
Irreducible representations and magnetic modes for $\boldsymbol{q}=(0, q_y, q_z)$ in *Pnma*.

Orbit I atoms: $Ho_{11}(x, y, z)$; $Ho_{12}(-x+1/2, y+1/2, z+1/2)$ Orbit II atoms: $Ho_{21}(-x,-y,-z)$; $Ho_{22}(x+1/2,-y+1/2,-z+1/2)$						
Irrep.	$(1\|0)$	$(m_x\|1/2,1/2,1/2)$	x	y	z	
Γ_1	1	ω	Fx	Ay	A_Z	$\omega=\exp(-\pi i(q_y+q_z))$
Γ_2	1	$-\omega$	Ax	Fy	Fz	
Atom						
1	1	2		⇐Permutation of atoms		
2	2	1[0 −1 −1]		and "returning" translations		

Table 3
Irreducible representations and magnetic modes for $\boldsymbol{q}=(q_x, q_y, 0)$ in *Pnma*.

Orbit I atoms: $Ho_{11}(x, y, z)$; $Ho_{12}(x+1/2, y, -z+1/2)$ Orbit II atoms: $Ho_{21}(-x,-y,-z)$; $Ho_{22}(x-1/2,-y, z-1/2$						
Irrep.	$(1\|0)$	$(m_z\|1/2,0, 1/2)$	x	y	z	
Γ_1	1	ω	Fx	Fy	Az	$\omega=\exp(-\pi i(q_x))$
Γ_2	1	$-\omega$	Ax	Ay	Fz	
Atom						
1	1	2		⇐Permutation of atoms		
2	2	1[0 −1 −1]		and "returning" translations		

Table 4
Refined structural and magnetic parameters in the paramagnetic and the magnetically ordered state from neutron data of the FeB-type HoSi compound. Space group *Pnma* (Nr. 62), all atoms at sites 4*c*: (x, 1/4, z).

HoSi	FeB-type (*Pnma*) 64.5%									
Parameter	26 K		2.7 K		10.9 K		17 K		20 K	
Atom	x	z	x	z	x	z	x	z	x	z
Ho	0.179(1)	0.117(1)	0.1773(8)	0.111(1)	0.1793(8)	0.114(1)	0.1793(9)	0.115(1)	0.1793(9)	0.115(1)
Si	0.043(2)	0.630(3)	0.040(2)	0.617(4)	0.040(2)	0.617(4)	0.035(2)	0.617(3)	0.035(2)	0.617(3)
a (Å), b (Å)	7.798(1)	3.7857(6)	7.823(2)	3.793(1)	7.820(2)	3.793(1)	7.821(2)	3.796(1)	7.821(2)	3.796(1)
c (Å)	5.619(1)		5.635(1)		5.635(1)		5.635(1)		5.632(1)	
$\boldsymbol{q}=(q_x, q_y, q_z)$			$\boldsymbol{q}_3=(0, q_y, q_z)$		$\boldsymbol{q}_3=(0, q_y, q_z)$		$\boldsymbol{q}_3=(q_x, q_y, q_z)$	$\boldsymbol{q}_4=(q_x, q_y, 0)$		$\boldsymbol{q}_4=(q_x, q_y, 0)$
q_x	–		0		0		0.010(2)	0.092(1)		0.099(1)
q_y			0.5271(2)		0.5275(2)		0.5274(5)	0.538(3)		0.5363(3)
q_z			0.0899(3)		0.0895(3)		0.090(1)	0		0
$\mu_{oy}(\mu_B)$	–		10.9(1)		10.9(2)		6.7(1)	6.7(1)		7.2(1)
φ_{12} (2π)			0.04(16)		−0.24(9)		−0.21(9)	−0.12(2)		−0.16(3)
φ_{21} (2π)			0.370(8)		0.24(1)		0.30(1)	0.29(1)		0.48(2)
φ_{22} (2π)			−0.33(15)		−0.51(9)		0.42(2)	0.49(3)		−0.36(3)
$\mu_{oT}(\mu_B)$, φ_b^o	–		10.9(1), 0		10.9(2), 0		6.7(1), 0	6.7(1), 0		7.2(1), 3(1)
R_B%, R_m%	4.9, –		2.3, 4.0		2.7, 3.8		2.7, 4.1	2.7, 4.8		3.0, 5.6
R_{wp}%, R_{exp}%, χ^2	18,16.3, 1.3		10, 4.0, 5.7		10.6, 6.0, 3		10.2, 3.6, 3.5		13.8, 7.2, 3.7	

μ_{ox} and μ_{oy} are the components of the refined Fourier coefficient parallel to *a*- and *b*-axes. μ_{oT} and φ_b are the amplitude of the wave and its angle with the *b*-axis. φ_{12}, φ_{21}, and φ_{22} are the phases for the sites Ho_{12} $(-x+1/2,-y+1/2, z+1/2)$, $Ho_{21}(-x,-y,-z)$ and Ho_{22} $(x+1/2, -y+1/2,-z+1/2)$ in fractions of 2π. R_B, R_{wp}, R_m% and R_{exp} are the Bragg factor, the reliability factor for the magnetic intensities, the weighted profile intensities, and the expected value related to the statistical accuracy of the data, respectively.

Icalc profiles. We first describe the HoSi CrB-type thermal behaviour and continue with the more complex FeB ordering.

3. Magnetic ordering of CrB-type compound HoSi

3.1. LT magnetic ordering of CrB-type HoSi: $\boldsymbol{q}_1=(1/2, 0, 1/2)$

The 2.7 K neutron powder pattern shown in the lower part of Fig. 1 displays a large number of additional strong magnetic contributions overwhelming the structural contributions that are present in the 26 K pattern shown in the upper part. In the low angle range $2\theta<30^\circ$ one may easily detect the CrB-type magnetic reflections (red dotted curve) associated with the wave vector $\boldsymbol{q}_1=(1/2, 0, 1/2)$ reported in [3,5]. The small magnetic peak around $2\theta=12^\circ$ labelled by (i) pertains to an unidentified impurity phase as it could not be indexed as a higher harmonic of the FeB-type structures see also next sections. This peak disappears below 11 K. The only resolved $\boldsymbol{q}_1$ magnetic peaks are (1/2, 1, 1/2) and (1/2, 2, 1/2) around 20° and 26° at 2.7 K, respectively. Their thermal behaviour is the only direct observation of the sequence of changes given in the next section and in Figs. 2 and 3.

The refined magnetic structure at 2.7 K is uniaxial with the Ho moments pointing along the shortest axis *c*. The moment direction changes sign along the t'_a and t'_c antitranslations and this leads to a two-fold cell enlargement in *a* and *c* directions, respectively. In the used model the Ho_1: (0, y, 1/4); Ho_2: (0, $-y$, 3/4) atoms contained in the primitive cell, at the 4*c* symmetry site of the

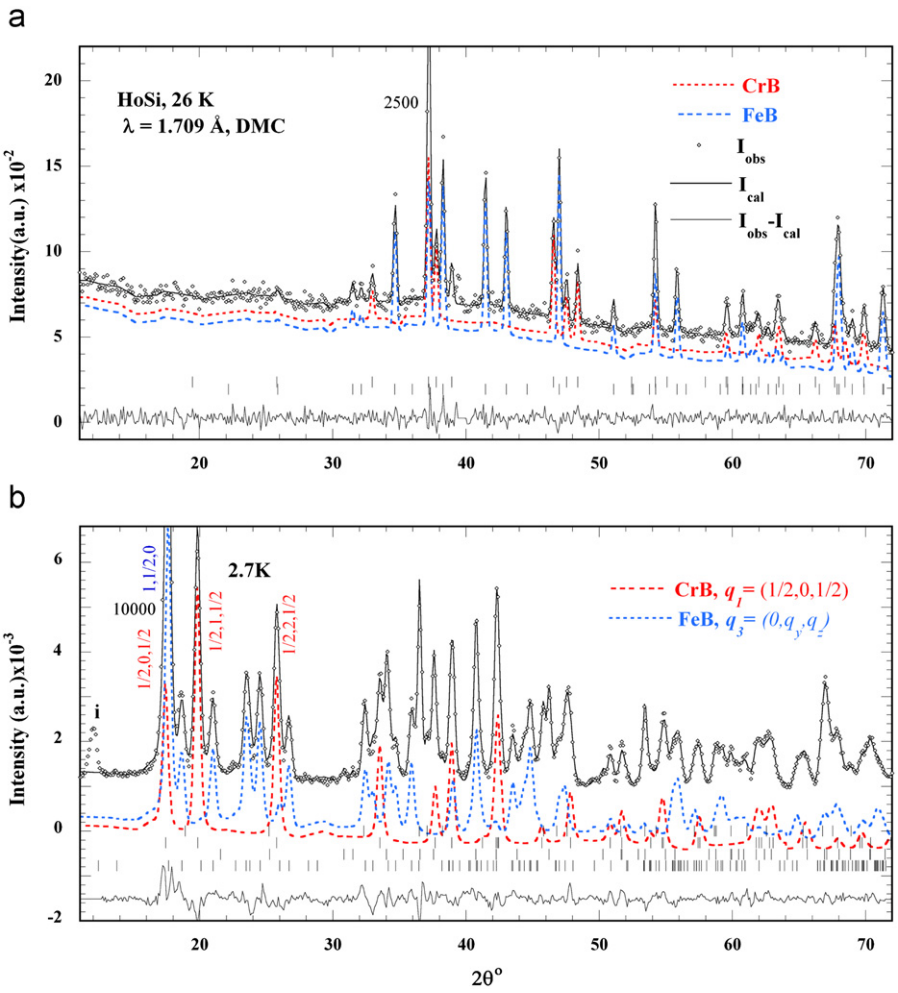

Fig. 1. Observed and calculated neutron diffraction patterns of the dimorphic HoSi compound (a) in the paramagnetic state at 26 K and (b) in the magnetically ordered state at 2.7 K with the wave vectors $\boldsymbol{q}_1=(1/2, 0, 1/2)$ for the CrB-type (*Cmcm*) and $\boldsymbol{q}_3=(0, 0.5271(2), 0.0899(3))$ for the FeB-type (*Pnma*). The individual calculated profiles (dotted curves) of structural at 26 K or magnetic origin at lower temperatures of the two structures are in red colour for the CrB phase and blue colour for the FeB phase. (For interpretation of the references to color in this figure legend, the reader is referred to the web version of this article.)

space group *Cmcm* (Nr. 62), belong to the same orbit and are symmetry related [3]; they have their moments in parallel. The moments of atoms 3 and 4 translated by (1/2, 1/2, 0) point in opposite directions.

The ordered moment value equals 8.6(2) μ_B/Ho^{3+} atom that is within error comparable to the 4.2 K value of 7.9(6) μ_B reported by us [5] for $HoGe_{0.2}Si_{0.8}$. These values fall below the free ion value ($g_J J\mu_B=10\,\mu B$ for Ho^{3+}), presumably due to crystal field effects. The small deviation of 5–7° of the Ho moments from the *c*-axis reported for the compounds with $x<1$ [5] and of 12° for $x=1$ [3] could not be confirmed for HoSi. A plot of the structure is given in Fig. 5, see the next section.

3.2. *HT magnetic ordering of CrB-type HoSi:* $\boldsymbol{q}_2=(q_{2x}, 0, q_{2z})$

The *LT* commensurate HoSi phase $\boldsymbol{q}_1$ remains stable with increase in temperature up to $T_{ic}=16.5$ K. Above T_{ic} the wave vector becomes incommensurate with the crystal lattice $\boldsymbol{q}_2=(q_{2x}, 0, q_{2z})$. Fig. 2 shows only minor changes between the *LT* 11 K and the *HT* 17 K data just above T_{ic}.

The commensurate→incommensurate CrB-type transition is best made visible by the change in distance (red line) between the (1/2, 1, 1/2) and (1/2, 2, 1/2) satellites at 11 K (lock-in phase) on heating, see Fig. 2(a). This distance between the two peaks, serving as a measure, decreases progressively with increase in temperature, the two satellites moving slightly in opposite directions (towards each other), see Fig. 2(b) and (c). At 17 K (Fig. 2(b)) the refinement (profile matching) led to an important change in the q_x component $\boldsymbol{q}_2=(0.4709(3), 0, 1/2)$. In view of the high complexity of the FeB *HT* ordering we have deleted in Fig. 2(b) the red dotted curve due to the CrB-type contributions present in the other parts of Fig. 2 as these show only minor changes.

As the $\boldsymbol{q}_1$ peak topology is not changing drastically, one may assume that there are only small changes of the wave vector components. More specific, as soon as q_z deviates from the lock-in value $q_z=1/2$, the (1/2, 1, 1/2) peak splits into the $\{1\,1\,0-\boldsymbol{q}_2, 1\,1\,1-\boldsymbol{q}_2\}$ satellites and the (1/2, 2, 1/2) peak splits into the $\{0\,2\,0\pm\boldsymbol{q}_2, 0\,2\,1-\boldsymbol{q}_2\}$ satellites. Contrary a q_x change will shift the two satellites in opposite directions but they will not split. Fig. 2(b) shows that at 17 K the (1/2, 1, 1/2) satellite moves to slightly higher and (1/2, 2, 1/2) to lower angles pointing to a q_x decrease, but there is no visible splitting pointing to a q_z change. In fact the satellite pairs become only resolved above $T>20$ K.

A minor q_z change was suggested by our refinements through the improvement of profile reliability factors above 18 K. The splitting of the $\boldsymbol{q}_1=(1/2, 0, 1/2)$ magnetic satellite into $\{000\pm\boldsymbol{q}_2, 001-\boldsymbol{q}_2\}$ for $q_z\neq 1/2$ is shown in Fig. 3 in a larger scale where we depicted the calculated CrB-type magnetic contributions of our best fits, below and above $T_{ic}=16.5$ K, and skip the overlapping FeB-type magnetic contributions (see Fig. 2). A temperature

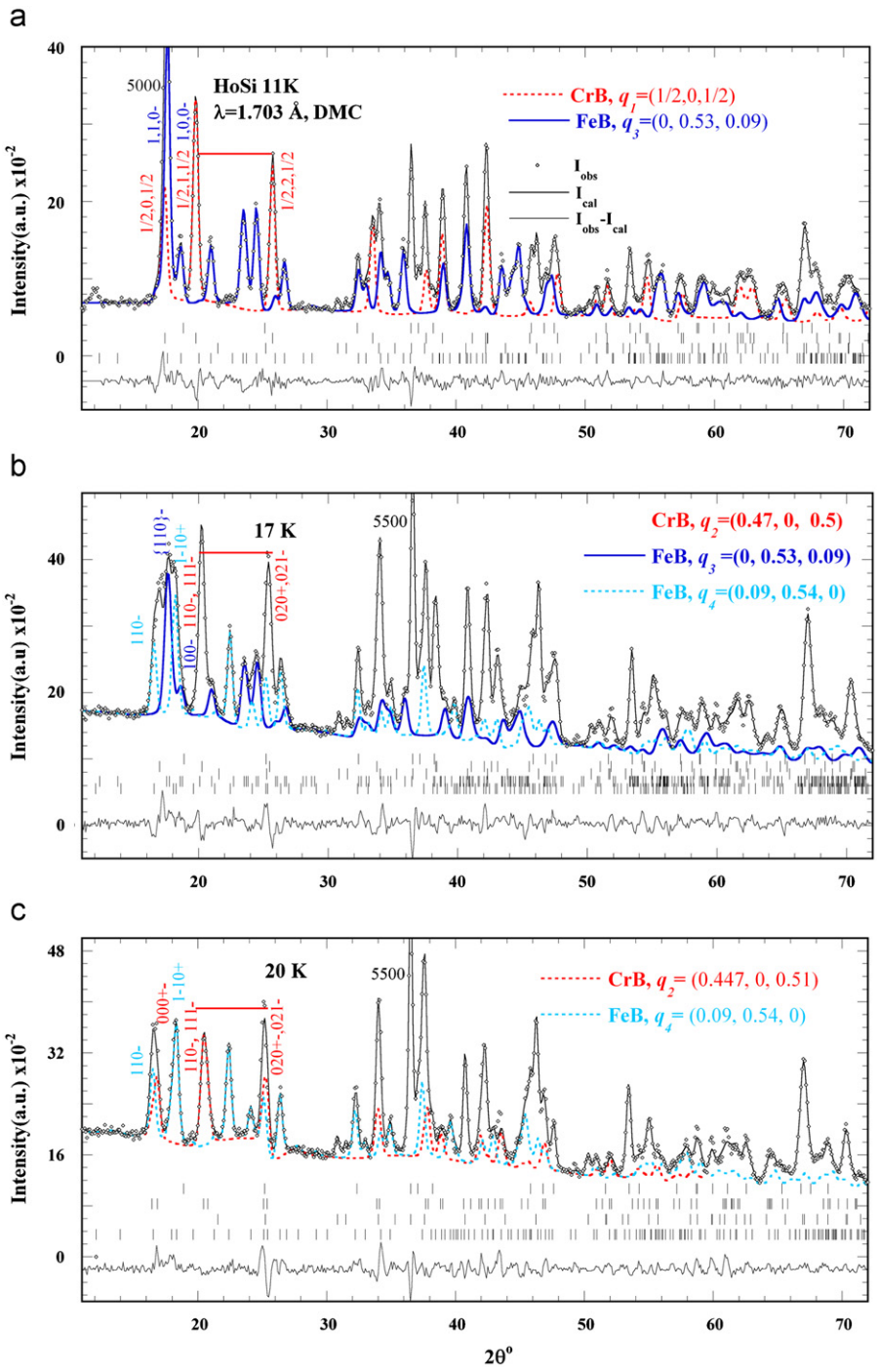

Fig. 2. A part of the observed and calculated neutron diffraction patterns of the dimorphic HoSi compound (a) in the (*LT*) magnetically ordered state at 10.9 K with $\boldsymbol{q}_1$=(1/2, 0, 1/2) for the CrB-type and $\boldsymbol{q}_3$=(0, 0.5275(2), 0.0895(3)) for the FeB-type, (b) in the intermediate range (*IT*) at 17 K with $\boldsymbol{q}_2$=(0.4709(3), 0, 1/2) for the CrB-type and two phases for the FeB-type $\boldsymbol{q}_3$=(0.010(2), 0.5274(5), 0.090(1)) (blue colour) and $\boldsymbol{q}_4$=(0.092(1), 0.538(1), 0) (cyan colour) and (c) in the *HT* range at 20 K with $\boldsymbol{q}_2$=(0.447(1), 0, 0.510(1)) for CrB (red colour) and $\boldsymbol{q}_4$=(0.099(1), 0.5363(1), 0) (cyan colour) for FeB. (For interpretation of the references to color in this figure legend, the reader is referred to the web version of this article.)

increase from 15 to 16 K affects the peak intensities but not their positions that remain almost unchanged below T_{ic}. In contrast at 17 K one observes a positional shift of (1/2, 0, 1/2) to lower 2θ locations compatible with a q_x change. At 18 K the visible peak asymmetry points to a small q_z change.

3.3. *T*-magnetic phase diagram of CrB-type HoSi

The temperature dependence of the wave vector components in Fig. 4(a) shows that the q_x component exhibits the largest change from 1/2 at T_{ic}=16.5 K to a smaller value 0.47 at 17 K, and continues to decrease up to T_N. This explains why the (1/2, 1, 1/2) peak shifts towards higher angles and the (1/2, 2, 1/2) peak towards lower angles in the incommensurate range. The five times smaller change of the q_z component becomes detectable only above 17 K.

The refined Ho magnetic moment amplitudes (Fourier coefficients) of the $\boldsymbol{q}_1$ and $\boldsymbol{q}_2$ phases given in Fig. 4(b) display a small discontinuity at the commensurate→incommensurate transition at T_{ic} deviating from the Brillouin-type behaviour. The ordered Ho

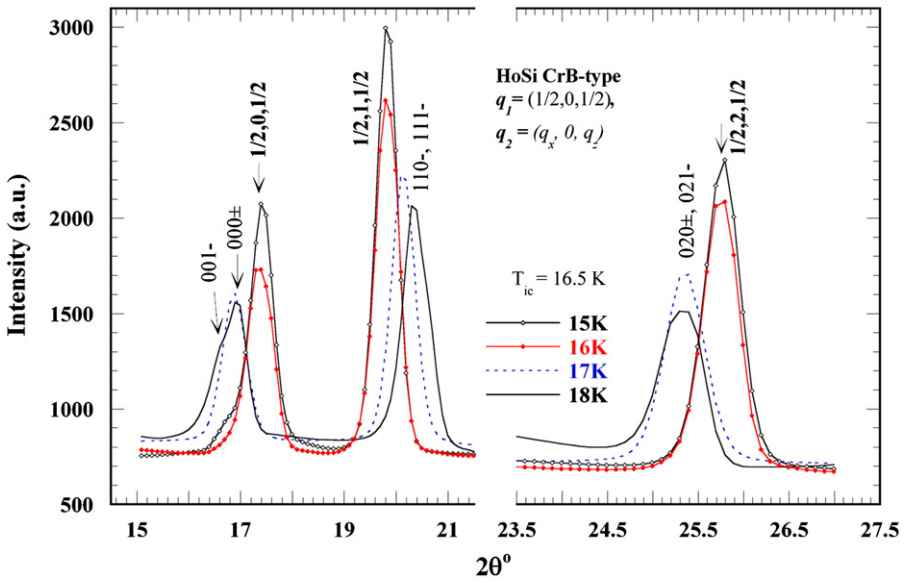

Fig. 3. The commensurate ($\boldsymbol{q}_1=(1/2, 0, 1/2)$) to incommensurate $\boldsymbol{q}_2=(q_x, 0, q_z)$ transition at $T_{ic}=16.5$ K in the CrB magnetic structure. Shown are the calculated profiles for four temperatures around T_{ic}.

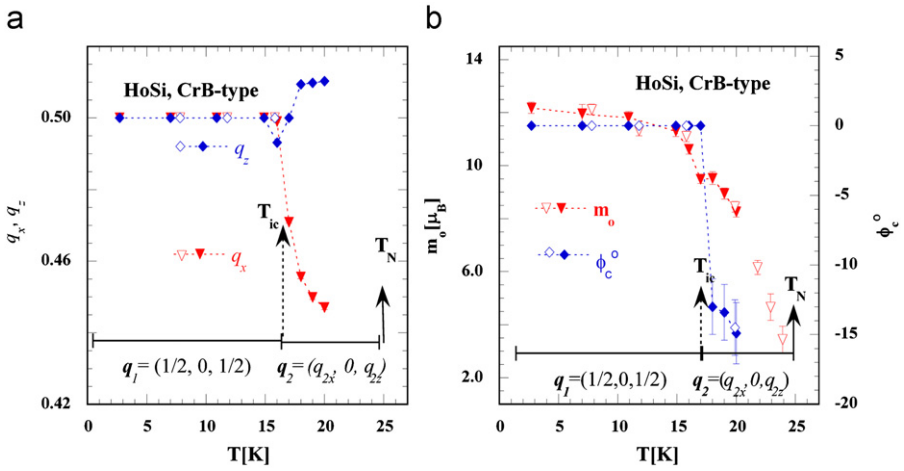

Fig. 4. T-dependence ($F(T)$) of the refined CrB-type magnetic parameters: (a) wave vector components $\boldsymbol{q}_2=(q_x, 0, q_z)$ and (b) Fourier coefficients or amplitude of the wave in the incommensurate phase. In the lock-in phase the Ho moment is obtained by scaling $m_o/\sqrt{2}$, the Fourier coefficients. Full and empty symbols of the same parameter correspond to data sets collected with different wavelengths.

equalling moment value in the lock-in state can be obtained from the Fourier coefficients by scaling with $1/\sqrt{2}m_o$ or adding a global phase of $\pi/4$ to the origin of the wave. Saturation is reached below 10 K where the ordered moment equals 8.6(2) μ_B/Ho atom. The moment orientation along the *c*-axis remains unchanged in the *LT* commensurate range (Fig. 4(b)). A small deviation of $-13^{\circ}(2)$ off the *c*-axis becomes detectable above T_{ic}.

Minor anomalies are also observed mainly in the lattice constant *a* at T_{ic}, which is the wave vector component that displays the largest change. Here we would like to state that possible minor structural changes connected to the symmetry lowering resulting from the magnetic transitions could not be refined, the data not being sensitive to possibly very small changes as often in powder data.

Fig. 4 serves also as T-magnetic phase diagram of the CrB-type HoSi compound as it defines the stability ranges of the two ordering types. HoSi displays the largest *LT* stability range with the commensurate phase $\boldsymbol{q}_1=(1/2, 0, 1/2)$ and the highest transition temperatures T_N and T_{ic} in the $HoGe_{1-x}Si_x$ (T, x) phase diagram system [5], confirming the trend of linear increase vs. x or that the system behaves like a solid solution.

The refined commensurate phase is shown for $2a\times 2c$ cells in a 3D plot in Fig. 5. In this model the atoms of the basis cell Ho_1: (0, *y*, 1/4); Ho_2: (0, $-y$, 3/4) belong to the same orbit and have their moments in parallel. Atoms Ho_3 and Ho_4 translated by (1/2, 1/2, 0) have their moment in opposite. A 2D-projection $2a\times 2c$ of the commensurate phase is compared in Fig. 6 with the incommensurate phase, see next section.

3.4. HT sinusoidal magnetic structure of CrB-type HoSi: $\boldsymbol{q}_2=(q_{2x}, 0, q_{2z})$

A sinusoidal modulated magnetic structure with an incommensurate wave vector in two directions as $\boldsymbol{q}_2=(q_{2x}, 0, q_{2z})$ corresponds to a change of the moment amplitude in the direction of the wave vector. In the perpendicular direction the moments have the same amplitude. Similar to the *LT* commensurate range just above the transition at 17 K with $\boldsymbol{q}_2=(0.4709, 0, 0.5)$ the moments point along the *c*-axis. The refined moment amplitudes (Fourier coefficients) in the basic unit cell are 9.5(2) μ_B/Ho atom (Table 1). The real structure may be derived

by Fourier expansion from the refined Fourier coefficients $\boldsymbol{S}_v(\boldsymbol{q}_j)$ by the expressions:

$$\boldsymbol{m}_v(\boldsymbol{R}_n)=\sum_{\{j\}}\boldsymbol{S}_v(\boldsymbol{q}_j)\exp(-2\pi i\boldsymbol{q}_j\boldsymbol{R}_n)=\sum_j \boldsymbol{S}_v^R(\boldsymbol{q}_j)\cos\{2\pi\boldsymbol{q}_j\boldsymbol{R}_n+\varphi_{jv}\} \quad (1)$$

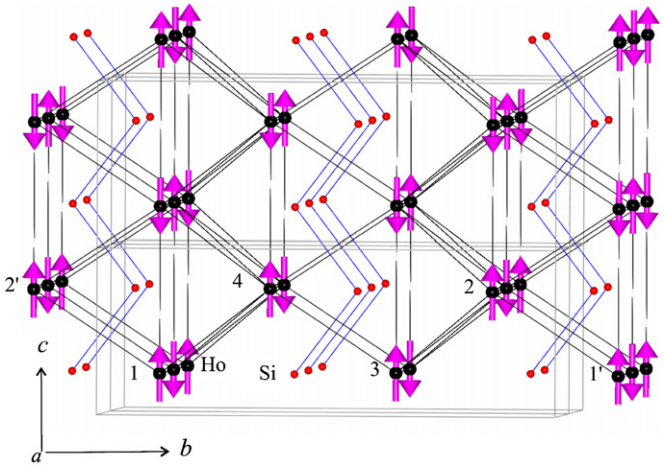

Fig. 5. 3D schematic representation of the commensurate $\boldsymbol{q}_1=(1/2,\ 0,\ 1/2)$ uniaxial HoSi phase of the CrB-type for $2a\times 2c$ cells. The Ho moments point along the shortest axis c at the corners of trigonal prisms centred by zigzag Si chains.

$$\boldsymbol{m}'_v(\boldsymbol{R}_n)=\sum_{\{j\}}\boldsymbol{S}_v(\boldsymbol{q}_j)\exp(-2\pi i\boldsymbol{q}_j\boldsymbol{R}_n+\Phi_{\{G\}})$$
$$=\sum_j \boldsymbol{S}_v^R(\boldsymbol{q}_j)\cos(2\pi i\boldsymbol{q}_j\boldsymbol{R}_n+\varphi_{jv}+\Phi_G) \quad (1')$$

$\boldsymbol{R}_{nv}=\boldsymbol{r}_v+\boldsymbol{R}_n$ here are the moment positions, $\boldsymbol{R}_n=n_1\boldsymbol{a}+n_2\boldsymbol{b}+n_3\boldsymbol{c}$ is a lattice translation vector with n_3 always being integer and (n_1, n_2) integer or simultaneously half integers (for the C-centred lattice); $\boldsymbol{r}_v$ is the vector position of the vth atom in the primitive unit cell (in our case $v=1, 2$). The first sum extends for all $(\boldsymbol{q}_j, -\boldsymbol{q}_j)$ pairs of the propagation vectors. The last sum assumes that the Fourier coefficients have the form $\boldsymbol{S}_v(\boldsymbol{q}_j)=1/2\ \boldsymbol{S}_v^R(\boldsymbol{q}_j)e^{-i\varphi_{jv}}$ so that after grouping the pairs $(\boldsymbol{q}_j,\ -\boldsymbol{q}_j)$, only the cosine terms are left. The expression (1′) indicates that a global phase Φ_G may be added to all the Fourier coefficients without changing the diffraction pattern. This parameter is not accessible to the experience and may give physically different magnetic structures in commensurate cases. The phases between atoms of the same orbit $\varphi_v(\boldsymbol{q}_j)=\varphi_{jv}$ are deduced by symmetry analysis from the basis functions of the representation [18]. These are usually products of the wave vectors by the translation part of the symmetry operators of $G_{\boldsymbol{q}}$ and/or returning translations. In commensurate phases these are fixed. If there is more than one orbit an additional phase between the orbits has to be refined because non-equivalent atoms are not related by symmetry. The 17 K magnetic moment arrangement for $(6a\times 3c)$ cells in Fig. 6(b) is compared to the commensurate phase (1/2, 0, 1/2) in Fig. 6(a).

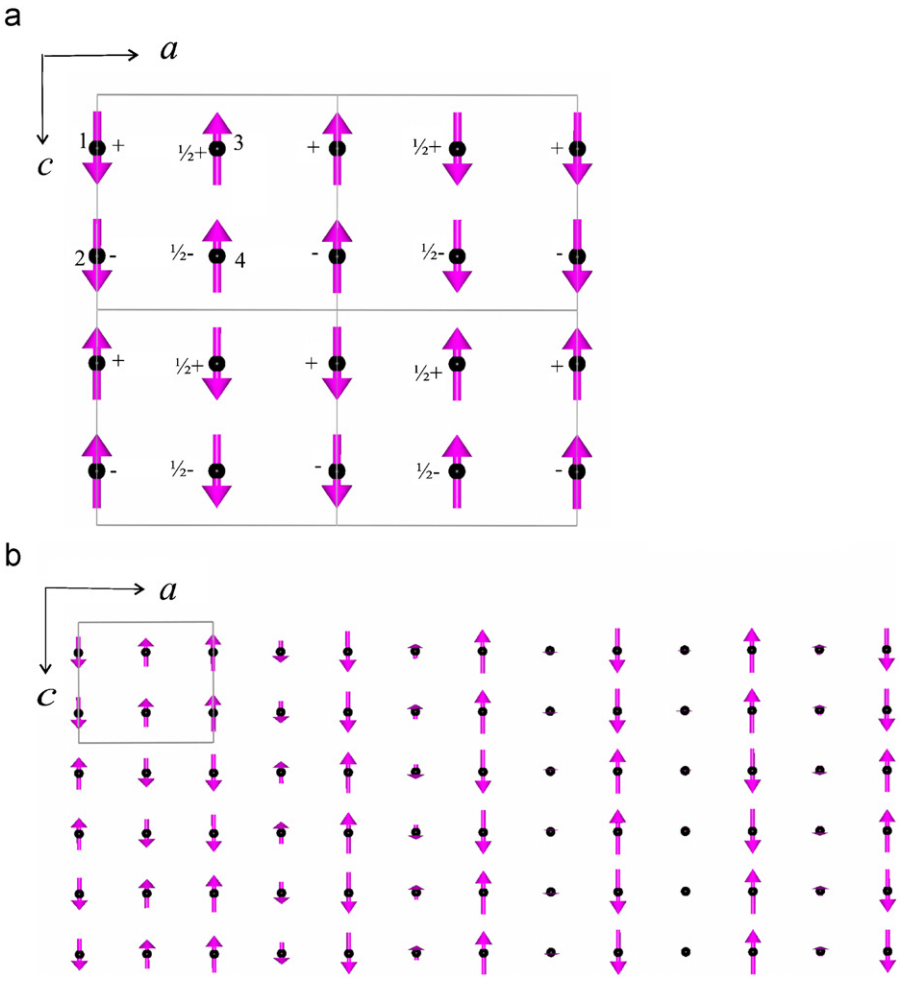

Fig. 6. 2D magnetic moment arrangement in the CrB-type HoSi compound within the plane (0 1 0) containing the wave vector (a) in the commensurate range for $2a\times 2c$ cells and (b) in the incommensurate range at 17 K $\boldsymbol{q}_2=(q_{2x}, 0, q_{2z})=(0.4709(3), 0, 1/2)$ for a large number of cells.

The 17 K refined $q_{2z}=1/2c^*$ commensurate component suggests that the $\boldsymbol{q}_1$ and $\boldsymbol{q}_2$ structures have the same arrangement of alternating moment sign along *c*. The moments of atoms Ho_1 and Ho_2 of the same orbit point to the same direction in both structures and are opposite to those of atoms 3 and 4 translated by (1/2, 1/2, 0) Fig. 6(a). The difference between the two arrangements is on the moment amplitude along the *a* direction because of the q_{2x} incommensurate value. Differences in the moment amplitudes of translation related atoms within the entire (0 1 0) plane become visible at 18 K as soon as $q_{2z}\neq 1/2$.

4. The magnetic ordering of the FeB-type HoSi compound

4.1. LT (2.7 K–T_{ic}) magnetic satellites of FeB-type HoSi: $\boldsymbol{q}_3=(0, q_{3y}, q_{3z})$

The magnetic peaks of FeB-type HoSi at 2.7 K (see Fig. 1) occur at reciprocal lattice positions requiring at least a two-fold cell enlargement along the shortest axis *b*. The first FeB-type reflection at $2\theta=18.2^\circ$, being located close to (1, 1/2, 0), suggests a wave vector close to (0, 1/2, 0). However the situation is more complex as this peak overlaps with a satellite of the coexisting CrB-type $\boldsymbol{q}_1=(1/2, 0, 1/2)$ phase. Therefore the exact wave vector value for FeB-type HoSi compound could be only derived by profile matching [15]. The *LT* FeB-type indexing has been greatly facilitated by the known commensurate CrB-type *LT* ordering and for the FeB-type by topological similarity with the isomorphic TbSi [8], CeSi [10,11] and DySi [12] compounds where two component wave vectors were also observed.

The best *LT* profile fit was obtained for a 2D incommensurate wave vector $\boldsymbol{q}_3=(0, 0.5271(2), 0.0899(3))$ close to $\boldsymbol{q}_3\approx(0, 9/17, 1/11)$. This wave vector explains all *LT* magnetic peaks next to those of the CrB type $\boldsymbol{q}_1$ set. The $\boldsymbol{q}_3$ magnetic contributions (blue dotted curve) in Figs. 1 and 2 are labelled as satellites of the main nuclear reflections $(h\,k\,l)$-$\boldsymbol{q}$ in blue colour.

In order to demonstrate the q_{3y} deviation from the commensurate value 1/2, we point to the splitting of the single satellite {1 1 0, 1 0 0}-$\boldsymbol{q}_3$, located at $2\theta=18.2^\circ$ for $q_{3y}=1/2$, into the satellites →(1 1 0)-$\boldsymbol{q}_3$ at 17.6° and (1 0 0)-$\boldsymbol{q}_3$ at 18.5°. The splitting is already detectable at 2.7 K, see Fig. 1(b), and does not change at higher temperatures, i.e. at 11 K (Fig. 2(a)) or 15 K (Fig. 7(a)). It depends exclusively on the q_{3y} deviation from 1/2.

The thermal evolution of the $\boldsymbol{q}_3=(0, q_{3y}, q_{3z})$ wave vector components in Fig. 8(a) shows that these remain almost unchanged within the *LT* range 2.7 K–T_{ic}. A similar thermal behaviour was found in DySi for the *LT* wave vector $\boldsymbol{q}$ close to ≈(0, 1/2, 1/11).

However, as will be shown in the next section, the *LT* peak topology of the FeB-type HoSi changes strongly at slightly higher temperatures, and these changes are different from those observed for DySi across the first order phase transition at $T_{ic}=16.5$ K. They are also in contrast to the minor CrB-type changes.

In conclusion the *LT* range 2.7–15 K of the FeB-type ordering is fully described by a two-dimensional incommensurate wave vector $\boldsymbol{q}_3=(0, q_{3y}, q_{3z})$ within the plane (1 0 0) that remains unchanged close to (0, 9/17, 1/11) with temperature.

4.2. The first-order transition in FeB-type HoSi at T_{ic}

4.2.1. Behaviour of FeB-type HoSi in the intermediate temperature range (16–17) K

The sequence of changes across the T_{ic} transition in dimorphic HoSi can easily be discerned by means of the enlarged scale used in Fig. 7, particularly in the low 2θ angle range comprising mainly magnetic contributions in a larger scale in Fig. 7. At 15 K (Fig. 7(a)) several CrB- and FeB-type satellites are described by the *LT* wave vectors $\boldsymbol{q}_1=(1/2, 0, 1/2)$ and $\boldsymbol{q}_3=(0, 0.527(2), 0.0899(3))$, respectively. At 16 K (Fig. 7(b)) additional and/or superimposed weak contributions to those of the $\boldsymbol{q}_1$ and $\boldsymbol{q}_3$ satellites appear at new locations (16.5°, 18.3°, 22.5° and 26.5°) denoted by arrows in Fig. 7(b) and (c) for the 16 and 17 K data, respectively. We recall that at this temperature in the CrB-type transition $\boldsymbol{q}_1=(1/2, 0, 1/2)\rightarrow\boldsymbol{q}_2=(q_{2x}, 0, q_{2z})$ the topological changes are of minor importance. The best 16 K profile matching was obtained assuming an additional 2D incommensurate wave vector $\boldsymbol{q}_4=(q_{4x}, q_{4y}, 0)$ within the (0 0 1) plane perpendicular to the *LT* vector $\boldsymbol{q}_3=(0, q_{3y}, q_{3z})$ (1 0 0). The weak intensity contributions of the new phase $\boldsymbol{q}_4$, as detected at 16 K (dotted cyan colour curve) in Figs. 2 and 7 next to the dominating $\boldsymbol{q}_3$ intensities, increase continuously on heating to 17 K at the cost of the $\boldsymbol{q}_3$ set. The coexistence range of the two magnetic phases is very narrow, just ±0.5 K around the T_{ic} 16.5 K transition. We note that in the intermediate temperature (*IT*) range $T_{ic}\pm 0.5$ K the $\boldsymbol{q}_3$ vector was refined assuming a general reciprocal lattice position to check for a possible intermediate *IT* three-dimensional incommensurate phase approaching the *HT* range as found in TbSi [8]. At 18 K the $\boldsymbol{q}_3$ satellites have fully disappeared and the *HT* range is described by the wave vector $\boldsymbol{q}_4$ and the peak topology is very similar to that at 20 K (Fig. 2(c)).

4.2.2. Magnetic satellites in the HT (T_{ic}–T_N) range of FeB-type HoSi: $\boldsymbol{q}_4=(q_{4x}, q_{4y}, 0)$

The *IT* range refinements 15–17 K of the HoSi FeB-type show (i) only minor changes of several $\boldsymbol{q}_3$ components and (ii) the presence of an additional symmetry independent vector $\boldsymbol{q}_4=(0.09, 0.538, 0)$ at 17 K. The presence of a q_{4x} component becomes evident by the thermal behaviour of the (1,1,0)-$\boldsymbol{q}_3$ FeB-type satellite located at $2\theta=17.5^\circ$ at 15 K, which at 17 K splits into the satellites $(1,-1,0)-\boldsymbol{q}_4$ at 16.5° and $(1,-1,0)+\boldsymbol{q}_4$ at 18.3° as soon as $q_x\neq 0$. The intensity of the $\boldsymbol{q}_4$ satellites displays already an important increase at 17 K at the cost of the $\boldsymbol{q}_3$ set that in fact fully disappears above 18 K cf. Fig. 2(c). The $\boldsymbol{q}_4$ components change more importantly than those of $\boldsymbol{q}_3$ with temperature. In Fig. 8(b), q_{4y} is seen to decrease and q_{4x} is seen to increase on heating. This corresponds to a small rotation of the wave vector within the plane (0 0 1) towards the *a*-axis as shown in Fig. 9.

Thus the *HT* range T_{ic}–T_N the magnetic ordering of the FeB-type HoSi compound is exclusively described by the symmetry independent wave vector $\boldsymbol{q}_4=(q_{4x}, q_{4y}, 0)$.

4.2.3. The magnetic phase diagram of FeB-type HoSi

The refined wave vector components over the entire magnetically ordered range are summarised in Fig. 10(a) that displays the FeB-type magnetic phase diagram in terms of wave vectors. In this figure the thermal evolution on heating of the $\boldsymbol{q}_3=(q_{3x}, q_{3y}, q_{3z})$ and $\boldsymbol{q}_4=(q_{4x}, q_{4y}, 0)$ vector components is shown together in a double *y*-scale plot. Their common component q_y (left vertical scale) is shown in red colour. Their q_x and q_z components (right vertical scale) are shown in green and blue colour, respectively. In principle these results are model independent; however, the plots refer to the full data analysis implementing a model choice that is discussed in the next section.

We mentioned already that in the *LT* range 2.7–15 K the q_{3x} and q_{3y} components show a very slight decrease and increase, respectively. The component q_{3z} remains unchanged. Also in the *IT* range where $\boldsymbol{q}_3$ exists as a metastable phase; it shows rather negligible changes between 16 K $\boldsymbol{q}_3=(0.0054(7), 0.5269(2), 0.0899(3))$ and 17 K $\boldsymbol{q}_3=(0.009(2), 0.5274(4), 0.090(1))$.

These facts indicate that with the used temperature window of 1 K in our experiment the wave vector $\boldsymbol{q}_3=(0.0054(7), 0.5269(2), 0.0899(3))$ at 16 K most likely jumps rather than rotates (in

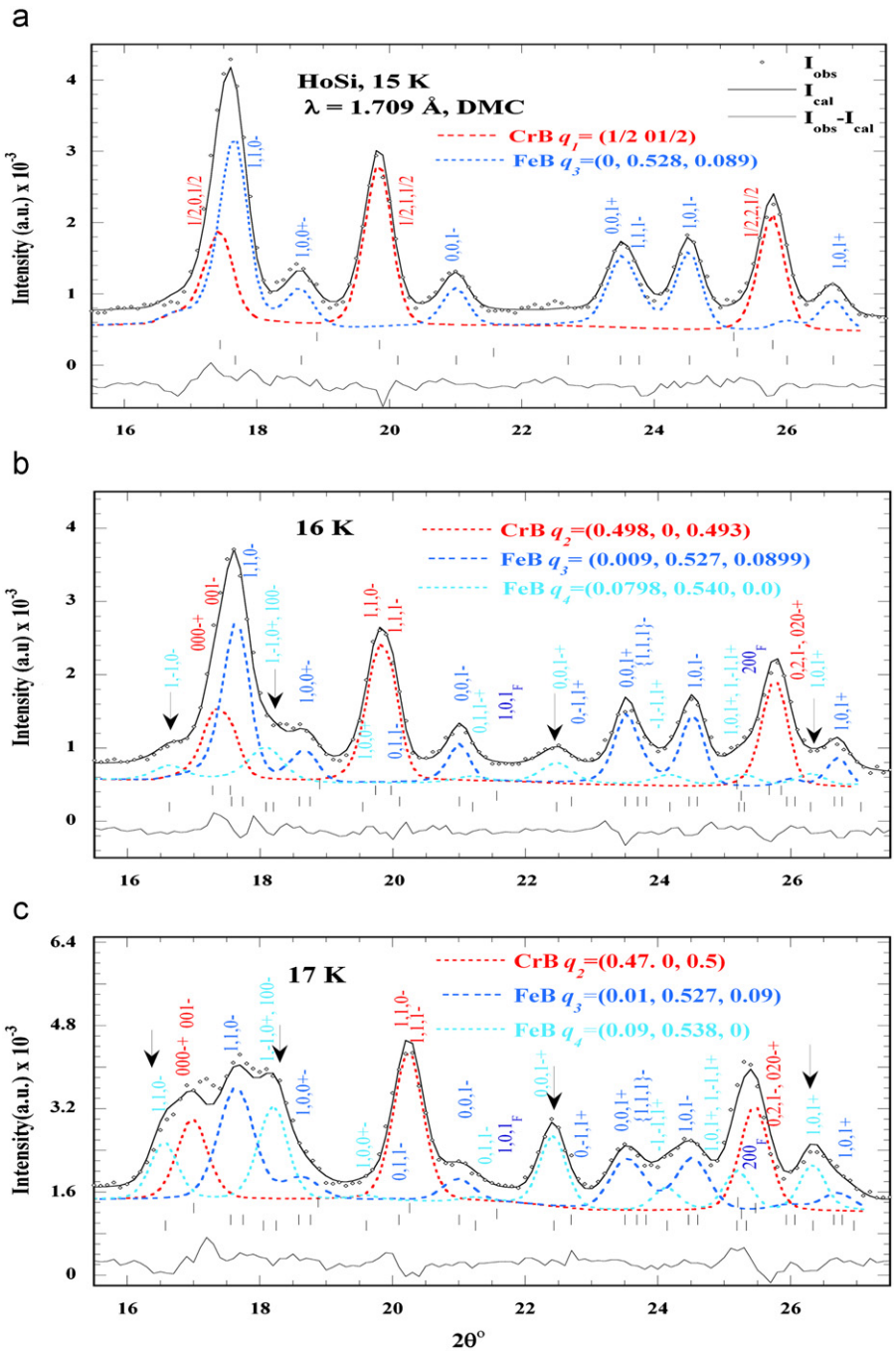

Fig. 7. A part of the observed and calculated neutron diffraction patterns of the dimorphic HoSi compound (a) in the (*LT*) magnetically ordered state at 15 K with $\boldsymbol{q}_1$=(1/2, 0, 1/2) for the CrB-type and $\boldsymbol{q}_3$=(0, 0.5275(2), 0.0895(3)) for the FeB-type, (b) in the intermediate range (*IT*) at 16 K with $\boldsymbol{q}_2$=(0.4709(3), 0, 1/2) for the CrB-type and two phases for the FeB-type $\boldsymbol{q}_3$=(0.010(2), 0.5274(5), 0.090(1)) (blue colour) and $\boldsymbol{q}_4$=(0.092(1), 0.538(1), 0) (cyan colour) and (c) in the *HT* range at 20 K with $\boldsymbol{q}_2$=(0.447(1), 0, 0.510(1)) for CrB (red colour) and $\boldsymbol{q}_4$=(0.099(1), 0.5363(1), 0) (cyan colour) for FeB. (For interpretation of the references to color in this figure legend, the reader is referred to the web version of this article.)

difference to TbSi [8]) at T_{ic} to the symmetry independent reciprocal lattice position $\boldsymbol{q}_4$=(0.079, 0.54, 0). In the *IT* range 16–17 K the $\boldsymbol{q}_3$ and $\boldsymbol{q}_4$ phases coexist as distinct phases in the form of domains with relative amounts varying with *T*. It is also possible that the transition takes place via an intermediate phase with two wave vectors, see also Section 4.4.

Thus the magnetic phase diagram in terms of wave vectors Fig. 10(a) comprises (in difference to the CrB-type diagram) three ranges of magnetic order: (i) *LT* (2.7 K–T_{ic}) with the wave vector $\boldsymbol{q}_3$=(0, q_{3y}, q_{3z}); (ii) *HT* (T_{ic}–T_N) with $\boldsymbol{q}_4$=(q_{4x}, q_{4y}, 0) and (iii) a very narrow intermediate temperature *IT* range $T_{ic}\pm0.5$ K (T_{ic}=16.5 K) where $\boldsymbol{q}_3$ and $\boldsymbol{q}_4$ coexist and where the portion of the $\boldsymbol{q}_4$ phase increases on heating at the cost of the $\boldsymbol{q}_3$ phase.

4.3. The magnetic refinements

4.3.1. The model choice for FeB-type HoSi

Various models have been developed for the FeB-type magnetic structures after the observation of the *LT* and *HT* symmetry-independent wave vectors $\boldsymbol{q}_3$=(0, q_{3y}, q_{3z}) and $\boldsymbol{q}_4$=(q_{4x}, q_{4y}, 0), respectively. These models are mainly based on the restrictions provided by symmetry analysis in terms of irreducible representations and their

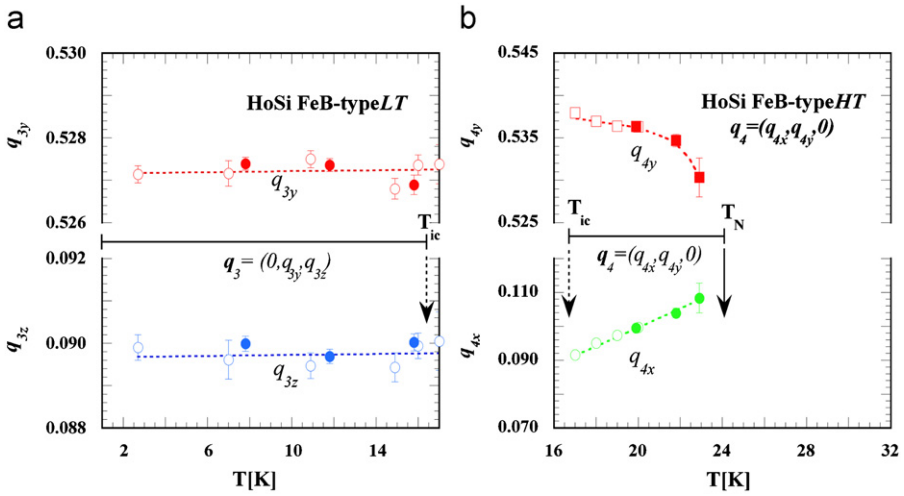

Fig. 8. Temperature dependence ($F(T)$) of the HoSi FeB-type phase refined: (a) wave vector components of the *LT* phase $\boldsymbol{q}_3=(0, q_{3y}, q_{3z})$ and (b) wave vector components of the *HT* phase $\boldsymbol{q}_4=(0, q_{4y}, q_{4z})$. Full and empty symbols of the same parameter correspond to data sets collected with a different wavelength.

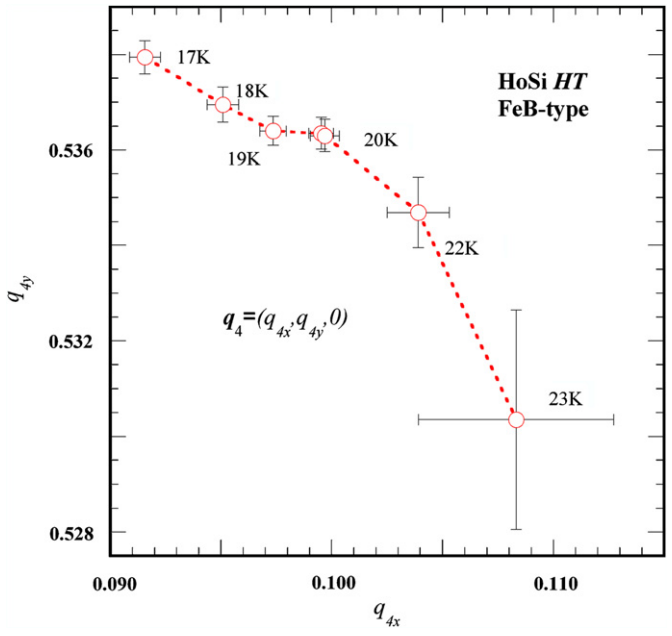

Fig. 9. q_x over q_y dependence with increase in temperature of the *HT* vector components $\boldsymbol{q}_4=(q_{4x}, q_{4y}, 0)$ of HoSi FeB-type, suggesting a rotation within the (0 0 1) plane. Full and empty symbols correspond to data points collected with a different wavelength.

linear combinations for the wave vectors $\boldsymbol{q}_3=(0, q_{3y}, q_{3z})$ and $\boldsymbol{q}_4=(q_{4x}, q_{4y}, 0)$ and the space group *Pnma*.

The magnetic atoms (Ho^{3+} ions) located at the 4*c* low symmetry site *m* of *Pnma* space group are labelled: Ho_1: (x, 1/4, z); Ho_2: ($-x+1/2$, 3/4, $z+1/2$); Ho_3: ($-x$, 3/4, $-z$); and Ho_4: ($x+1/2$, 1/4, $-z+1/2$).

Under the action of the wave vector $\boldsymbol{q}_3=(0, q_3, q_{3z})$ the 4*c* site in the *Pnma* space group splits into two orbits. Orbit I comprises atoms 1 and 2 (Ho_{11} and Ho_{12}) related by the glide plane n_x symmetry operation, and orbit II atoms 3 and 4 (Table 2). For the $\boldsymbol{q}_3$ wave vector and space group *Pnma* we refer to a full symmetry analysis given in [12] for the isomorphic DySi compound.

Under the action of the wave vector $\boldsymbol{q}_4=(q_{4x}, q_{4y}, 0)$ the 4*c* site in *Pnma* space group splits similarly to $\boldsymbol{q}_3$ also into two orbits. However as the $\boldsymbol{q}_3$ and $\boldsymbol{q}_4$ vectors are symmetry independent the splitting of the 4*c* site leads to orbits that comprise different Ho

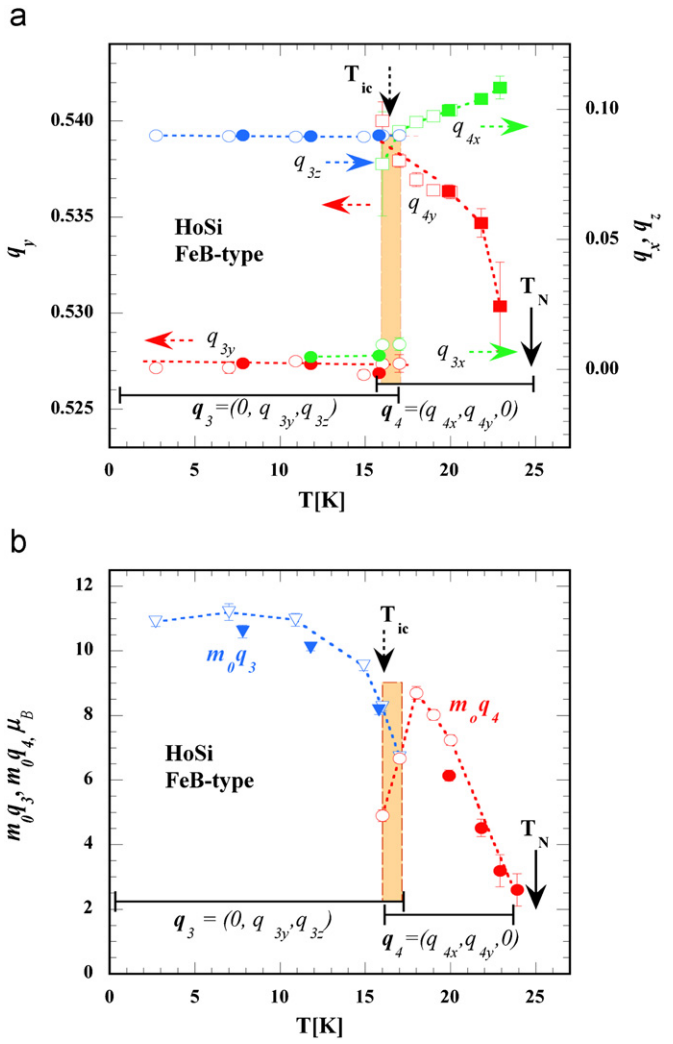

Fig. 10. Temperature dependence of the FeB-type (a) *LT* $\boldsymbol{q}_3=(0, q_{3y}, q_{3z})$ and *HT* $\boldsymbol{q}_4=(0, q_{4y}, q_{4z})$ wave vector components shown in a double *y*-scale. A narrow coexistence range is shown in orange colour and (b) of the refined Fourier coefficients or amplitude of the sine wave *LT* and *HT* incommensurate $\boldsymbol{q}_3$ and $\boldsymbol{q}_4$ phases, respectively. Full and empty symbols of the same parameter correspond to data sets collected with a different wavelength. (For interpretation of the references to color in this figure legend, the reader is referred to the web version of this article.)

atom pairs. For the $\boldsymbol{q}_4$ vector (Table 3) orbit I comprises atoms Ho_1 and Ho_4 (Ho_{11} and Ho_{12}) at layer $y=1/4$ related by the glide plane a_z operation and orbit II the atoms Ho_2 and Ho_3 (Ho_{21} and Ho_{22}) at layer $y=3/4$.

The Fourier coefficients and phases of atoms of the same orbit are symmetry related while atoms of different orbits may have various values and orientations. The models used in the refinements of the $\boldsymbol{q}_3$ and $\boldsymbol{q}_4$ phases are obtained from the basis functions given in Tables 2 and 3 of the relevant representations by applying the projection operator formula.

For the *LT* range with the wave vector $\boldsymbol{q}_3$ the Γ_1 representation results in the magnetic modes *Fx*, *Ay* and *Az* [12]:

$$S_{1x}+bS_{2x}=Fx,\quad S_{1y}-bS_{2y}=Ay,\quad S_{1z}-bS_{2z}=Az\ (\text{with}\ b=e^{-2\pi i(q_y+q_z)})$$

for the Γ_2 representation one obtains the modes *Ax*, *Fy* and *Fz*:

$$S_{1x}-bS_{2x}=Ax,\quad S_{1y}+bS_{2y}=Fy,\quad S_{1z}+bS_{2z}=Fz\ (\text{with}\ b=e^{-2\pi i(q_y+q_z)})$$

For the *HT* range with the wave vector $\boldsymbol{q}_4$ the Γ_1 representation results in the magnetic modes *Fx*, *Fy* and *Az*:

$$S_{1x}+bS_{2x}=Fx,\quad S_{1y}+bS_{2y}=Fy,\quad S_{1z}-bS_{2z}=Az\ (\text{with}\ b=e^{-2\pi i(qx)})$$

For the Γ_2 representation one obtains the modes *Ax*, *Ay* and *Fz:*

$$S_{1x}-bS_{2x}=Ax,\quad S_{1y}-bS_{2y}=Ay,\quad S_{1z}+bS_{2z}=Fz\ (\text{with}\ b=e^{-2\pi i(q_y+q_z)})$$

In conclusion symmetry analysis has shown that for both wave vectors $\boldsymbol{q}_3=(0, q_{3y}, q_{3z})$ and $\boldsymbol{q}_4=(q_{4x}, q_{4y}, 0)$, the space group *Pnma* would allow canted structures with three components and two different modes (planar canting) for the low symmetry rare earth site 4*c* (m).

4.3.2. Magnetic structures for FeB-type HoSi: $\boldsymbol{q}_3=(0, q_{3y}, q_{3z})$ LT and $\boldsymbol{q}_4=(q_{4x}, q_{4y}, 0)$ HT

As higher harmonics were not observed for either of these wave vectors the refinements used a sinusoidal model for the $\boldsymbol{q}_3$ FeB-type *LT* as well as for the $\boldsymbol{q}_4$ *HT* magnetic phases. The weak magnetic peak at 12° observed in the *LT* range Fig. 1(b) up to 11 K could not be identified as the third harmonic $3\boldsymbol{q}_3$ of the *LT* vector. The available information does not allow to distinguish between more complex models requiring further vectors or of an unknown magnetic impurity. The refinements relay on the second possibility. The best data fit was obtained for both vectors for uniaxial amplitude modulated magnetic structures with the magnetic moments oriented along the *b* direction at any temperature.

For the *LT* $\boldsymbol{q}_3$ phase the best fit was obtained for the $F_y=S_{1y}+bS_{2y}$ mode according to the Γ_2 representation where $b=e^{-2\pi i(qy+qz)}$ and S_{1y} and S_{2y} are the Fourier coefficients of the atoms of orbit I: Ho_1: $(x, 1/4, z)$; Ho_2: $(-x+1/2, 3/4, z+1/2)$ as given in Table 2. At 2.7 K the refined amplitude is 10.9(1) μ_B/Ho^{3+} and $\boldsymbol{q}_3$ is incommensurate with the crystal lattice in two dimensions $\boldsymbol{q}_3=(0, 0.5271(2), 0.0899(3))$, close to (0, 9/17, 1/11). Results for two *LT* range temperatures and at 17 K (*IT* range) where $\boldsymbol{q}_3$ exists as a metastable phase are given in Table 4 together with those of $\boldsymbol{q}_4$.

As already mentioned, the *HT* $\boldsymbol{q}_4=(q_x, q_y, 0)$ satellites were first observed at 16 K, together with the $\boldsymbol{q}_3$ *LT* satellites in the narrow *IT* range. The best data fit for the $\boldsymbol{q}_4$ phase over the *HT* and *IT* ranges was obtained for the same model with the $F_y=S_{1y}+bS_{2y}$ mode according to the Γ_1 representation. The parameter $b=e^{-2\pi i(qx)}$ in Table 3 depends only on the q_{4x} component. S_{1y} and S_{2y} are the Fourier coefficients of the 4*c* Ho atoms of orbit I: Ho_1: $(x, 1/4, z)$; Ho_4: $(x+1/2, 1/4, -z+1/2)$. Orbit II comprises the atoms Ho_2 and Ho_3.

The 17 K refinement (*IT* range) led to the incommensurate wave vectors $\boldsymbol{q}_3=(0.010(2), 0.5274(5), 0.0899(3))$, being close to $\approx(1/100, 9/17, 1/11)$ and $\boldsymbol{q}_4=(0.092(1), 0.538(3), 0)$ close to (1/11, 8/15, 0) values. Incidentally at this temperature the refined amplitudes for both vectors are the same 6.7(1) μ_B/Ho^{3+}. The refined parameters for characteristic temperatures in the three temperature ranges are given in Table 4. The low reliability factors support the model choice made for both structures.

Both $\boldsymbol{q}_3$ and $\boldsymbol{q}_4$ structures correspond to sinusoidal modulations with the local moment orientation fixed along the shortest axis *b*, presumably through the crystal field anisotropy. The ordered Ho^{3+} moment value derived by expression (1) depends on the position of the atom and may vary between 0 and m_{oj} in the direction of the wave vector. This can be seen in Fig. 11 for the *LT* phase at 2.7 K for the wave vector $\boldsymbol{q}_3=(0, 1/2, 1/11)$ for a large number of cells ($a\times 6b\times 6c$), and Fig. 12 shows the situation for $\boldsymbol{q}_4=(0.092(1), 0.538(3), 0)$ at 17 K for ($12a\times 6b\times c$) cells.

In Figs. 11 and 12 the magnetic moments of Ho atoms of the same orbit are given the same colour. Both structures are viewed along a direction perpendicular to the plane of the corresponding 2D wave vector, being (1 0 0) for the $\boldsymbol{q}_3$ structure in Fig. 11 and (0 0 1) for $\boldsymbol{q}_4$ in Fig. 12. What is common in both structures beside the moment direction is that the ordered moment value is close to zero at certain locations. In this view there exist even ranges where one colour prevails and the other colour is almost not visible, see the rectangular frame (dotted line) in Fig. 12. This suggests that even at low temperatures within certain ranges in the crystal, the Ho moments can be considered as quasi-disordered.

4.3.3. Thermal evolution of the Sq_3 and Sq_4 Fourier coefficients

The thermal variation of the calculated $\boldsymbol{q}_3$ and $\boldsymbol{q}_4$ Ho magnetic amplitudes (Fourier coefficients) is shown in Fig. 10(b). The $\boldsymbol{q}_3$ amplitude remains unchanged below the saturation temperature 10 K (10.9 μ_B/Ho^{3+}) decreases quite fast above 10 K and drops to zero towards $T_{ic}=16.5$ K simultaneously with the appearance of the $\boldsymbol{q}_4$ satellites. The amplitude of the $\boldsymbol{q}_4$ wave decreases smoothly above T_{ic} to T_N. Figs. 10(b) and 10(a) can be regarded as the T-magnetic phase diagram as they show the stability ranges of the $\boldsymbol{q}_3$ and $\boldsymbol{q}_4$ phases. Beside the paramagnetic range the HoSi FeB-type phase diagram comprises three ranges of magnetic order: (i) the *LT* 2.7 K–T_{ic} range with the wave vector $\boldsymbol{q}_3=(0, q_{3y}, q_{3z})$, (ii) the *HT* range T_{ic}–T_N with the wave vector $\boldsymbol{q}_4=(q_{4x}, q_{4y}, 0)$, and (iii) the narrow intermediate range *IT* ± 0.5 K around $T_{ic}=16.5$ K where the two structures coexist in varying amounts.

4.4. Multiple $\boldsymbol{q}$-vectors incommensurate phase ($\boldsymbol{q}_3$, $\boldsymbol{q}_4$) at 17 K for FeB-type HoSi

Symmetry analysis has shown that under the action of the symmetry independent *LT* and *HT* wave vectors $\boldsymbol{q}_3=(0, q_{3y}, q_{3z})$ and $\boldsymbol{q}_4=(q_{4x}, q_{4y}, 0)$, respectively, of *Pnma* space group, the 4*c* Ho site splits into two orbits that harbour different Ho atom pairs as given in Section 4.3.1 and in Tables 2 and 3.

In the previous sections we assumed that in the intermediate range *IT* the *LT* $\boldsymbol{q}_3$ and *HT* $\boldsymbol{q}_4$ competing phases shown in Figs. 11 and 12 coexist in the form of distinct magnetic domains. However in the *IT* range one may face a model where the vectors $\boldsymbol{q}_3$ and $\boldsymbol{q}_4$ act on the same physical space and give rise to a distinct multiple $\boldsymbol{q}$-vectors magnetic structure.

Such a possibility cannot be excluded by our experiment as it is known that Fourier coefficients $\boldsymbol{S}_v(\boldsymbol{q}_j)$ are in general complex vectors with six components and the phase between them cannot be found by diffraction. This is a general problem of diffraction of multiple $\boldsymbol{q}$-vectors structures [18,19] between the Fourier coefficients of independent wave vectors because they give rise to reflections at different locations and there is no interference between them so that the phase factor cannot be estimated.

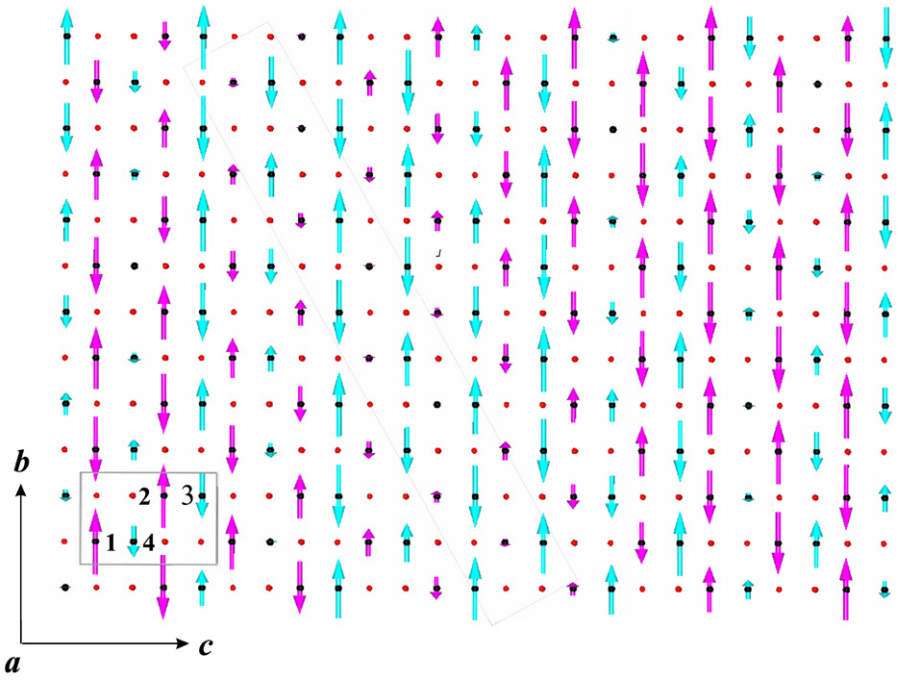

Fig. 11. HoSi FeB-type magnetic structure with the wave vector $\boldsymbol{q}_3$=(0, 0.5271(2), 0.0899(3)) at 2.7 K for (a, 2b, 11c) cells. The magnetic moments point to the b-axis. The Ho nearest- and next nearest neighbours are located at the corners of a trigonal Ho prism, i.e. the six atoms around Ho_1' in Fig. 3 (Ho_2, Ho_3, Ho_2' and those translated by $-t_b$ are antiferromagnetically coupled). This arrangement results to a zero molecular field at Ho_1'.

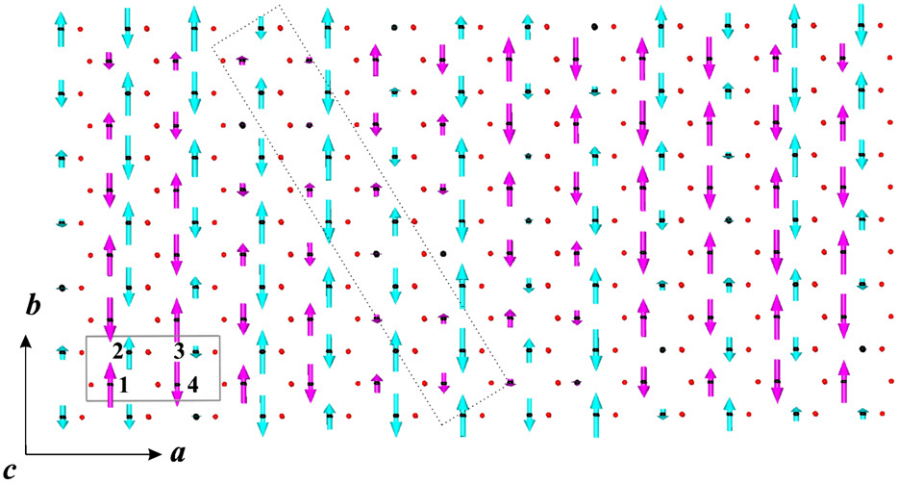

Fig. 12. HoSi FeB-type *HT* incommensurate magnetic structure at 17 K with the wave vector $\boldsymbol{q}_4$=(0.092, 0.538, 0) shown for (11a, 2b, c) cells. The magnetic moments are oriented along the b-axis. The Ho atoms are surrounded by 10 Ho and 7 Si atoms. (For interpretation of the references to color in this figure legend, the reader is referred to the web version of this article.)

As a consequence one cannot distinguish between coexisting magnetic domains of several single-$\boldsymbol{q}$ or multiple $\boldsymbol{q}$-vectors structures. A further ambiguity arises by the addition of a non-symmetry defined Global phase Φ_G in Eq. (1) depending on $\boldsymbol{q}$ that modifies the magnetic structure through origin shifts of the $\boldsymbol{q}$ waves, without changing the magnetic intensities. This would lead to infinity of multiple $\boldsymbol{q}$-vectors magnetic structures. Similar ambiguities exist in powder neutron diffraction for canted magnetic structures with symmetry higher than orthorhombic [20].

For commensurate phases there is a numerical phase optimisation using the program "Moment" [21] to derive structures minimising the magnetic moment fluctuations within a region of the crystal. For incommensurate sine wave magnetic structures the addition of a global phase may only have an influence on the moment fluctuations in a small part of the crystal and not in a larger area, as the structure remains incommensurate.

In FeB-type HoSi symmetry analysis has shown a different symmetry lowering under the action of the vectors $\boldsymbol{q}_3$ and $\boldsymbol{q}_4$ on *Pnma*. The 4*c* Ho site splits in both cases into two orbits that comprise different Ho atom pairs, therefore it is trivial to assume that in the *IT* range for a multiple $\boldsymbol{q}$-vectors structure there is no symmetry left and consequently the Ho 4*c* site splits in to 4 orbits shown by different colours in Fig. 13. The resulting ordered Ho moment value is obtained by combining the Fourier coefficients $\boldsymbol{S}_v(\boldsymbol{q}_3)$ and $\boldsymbol{S}_v(\boldsymbol{q}_4)$.

In the *IT* range both structures have collinear arrangements. All $\boldsymbol{S}_v(\boldsymbol{q}_j)$ vectors point along b; consequently also the magnetic moments are along b. Then the moments of the vth atom in the

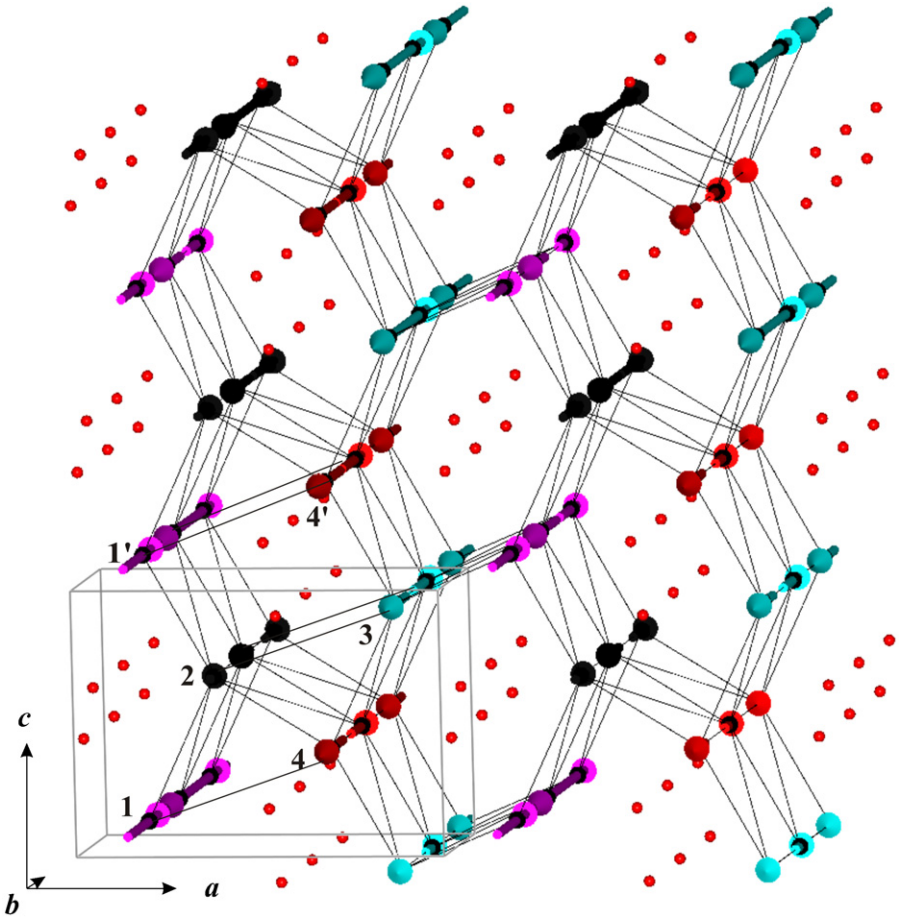

Fig. 13. HoSi FeB-type *IT* 3D incommensurate multiple $\boldsymbol{q}$-vectors collinear magnetic structure at 17 K under the assumption that the wave vectors $\boldsymbol{q}_3=(0,\ q_{3y},\ q_{3y})$ and $\boldsymbol{q}_4=(q_{4x},\ q_{3y},\ 0)$ act on the same physical space. The 4*c* Ho site is split into 4 orbits shown by different colours with their moments pointing to the *b*-direction. (For interpretation of the references to color in this figure legend, the reader is referred to the web version of this article.)

*n*th cell $\boldsymbol{m}_\nu(\boldsymbol{R}_n)$ can be found by rewriting formula (1) for the vectors $\boldsymbol{S}\nu_{\boldsymbol{qj}}$ and the total phase:

$$\boldsymbol{m}_\nu(\boldsymbol{R}_n)=\boldsymbol{S}_\nu(\boldsymbol{q}_3)\cos(2\pi\boldsymbol{q}_3\boldsymbol{R}_n+\Psi\boldsymbol{q}_3 s)+S_\nu(\boldsymbol{q}_4)\cos(2\pi\boldsymbol{q}_4\boldsymbol{R}_n+\Psi\boldsymbol{q}_4 s) \tag{2}$$

$$\Psi_{\boldsymbol{qjs}}=\Phi_{G\boldsymbol{qs}}+\varphi_{\boldsymbol{qjs}}$$

The total phase factor has two components: $\Psi_{\boldsymbol{qjs}}=\Phi_{\boldsymbol{qj}}+\varphi_{\boldsymbol{qjs}}$ where the global phase factor $\Phi_{\boldsymbol{qj}}$ not determined by symmetry and is a free parameter and that is significant only for an independent set of magnetic atoms (one orbit) with respect to another one. The component $\varphi_{\boldsymbol{qjs}}$ given in Table 3 is a phase factor determined by symmetry.

The resulting 3D multiple-$\boldsymbol{q}$ vectors incommensurate structure is collinear as the vectors $\boldsymbol{S}_\nu(\boldsymbol{q}_3)$ and $\boldsymbol{S}_\nu(\boldsymbol{q}_4)$ point into the same direction but the 4Ho moments may have different amplitudes. The global phase factor for the $\boldsymbol{Sq}_3$ and $\boldsymbol{Sq}_4$ coefficients in the 3D structure shown in Fig. 13 is set to zero. In this figure the rectangular side (Ho atoms 1′, 4′, 2 and 3) of the rare trigonal prism arrangement comprises one atom of each orbit. Within a slab from $y=0$–0.5 perpendicular to the *b*-axis for $14a\times17c$ cells comprising at $y=1/4$ the Ho_1 (magenta) and Ho_4 (red) moments, Fig. 14(a), and a slab from $y=0.5$–1 with Ho_2 (black) and Ho_3 (cyan) moments at $y=3/4$, Fig. 14(b), one obtains the impression that the space is subdivided into two magnetically ordered oval regions (coloured) alternating with magnetically disordered oval regions (white). In fact these regions span in three dimensions as the q_y vector components are also incommensurate.

5. Discussion

A comparison of the two structure types involved in the presently investigated dimorphic HoSi compound was given in three dimensions in [17] on the basis of X-ray single crystal data at 293 K. The CrB-type has a slightly larger cell volume than the FeB-type. As the two compounds have the same chemical formula this indicates a difference in the bonding as suggested on the basis of differences in the valence electron concentration of the 4*f* and 5*d* shells of the rare earth metals of the two modifications [22]. Our results confirm the findings of [17] concerning the cell volume also at lower temperatures down to 2.7 K. Below we will discuss the two concomitant magnetic ordering phenomena in the two structures in more detail and compare them with those in other *R*Si compounds as far as available.

We have shown that the CrB-type T-magnetic HoSi phase diagram (Fig. 4(a)) comprises an *LT* commensurate $\boldsymbol{q}_1=(1/2,\ 0,\ 1/2)$ phase stable up to $T_{ic}=16.5$ K, and an *HT* incommensurate $\boldsymbol{q}_2=(q_x,\ 0,\ q_z)$ phase stable up to $T_N=25$ K. The HoSi transition temperatures T_{ic} and T_N are the highest observed in the $HoGe_{1-x}Si_x$ (T, x) magnetic phase diagram, confirming the trend of linear increase of the *LT* and *HT* stability ranges with increase in T and x ($0\le x\le1$). The same applies for the behaviour of lattice constants and the cell volume decreasing linearly with increase in x, the *c*-axis displaying the largest decrease and the *b*-axis the second largest decrease while *a* remains almost unchanged. Also the thermal behaviour of the q_x, q_z wave vector components that change in opposite directions, the former being 5x times faster than the latter, is in full agreement with the

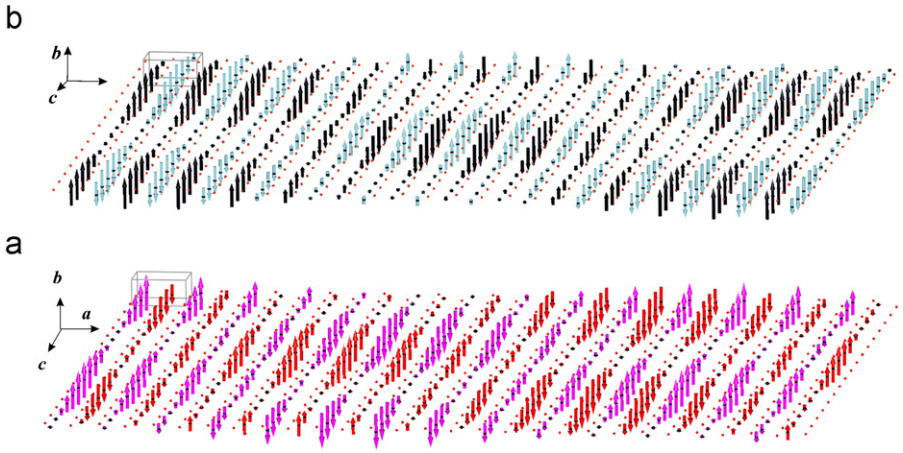

Fig. 14. The magnetic moment arrangement within a slab from $y=0$–0.5 and $y=0.5$–1 perpendicular to the b-axis for $14a\times17c$ cells in the multiple-$\boldsymbol{q}$ vectors HoSi structure comprising at $y=1/4$ the Ho_1 (magenta) and Ho_4 (red) moments, (a), and Ho_2 (black) and Ho_3 (cyan) moments at $y=3/4$, Fig. 14(b). One obtains the impression that the space is subdivided into ordered oval regions (coloured) alternating with disordered oval regions (white). Actually the regions span in 3D also along the b-axis that became incommensurate. (For interpretation of the references to color in this figure legend, the reader is referred to the web version of this article.)

trend of the series [5]. The magnetic moment deviation of 2–5° from the c-axis found for $x<1$ compositions is not observed in the HoSi at *LT*.

In conclusion the linear dependence of several relevant physical parameters with regard to the magnetic ordering of the CrB-type HoSi compound including T_N and T_{ic} on T, x, confirm the behaviour of solid solution of the pseudo-binary $HoGe_{1-x}Si_x$, (T, x) magnetic system and provides the missing *HT* information of the end member $x=1$ in the phase diagram. Replacing silicon for germanium has the effect of chemical pressure.

Trying to understand the relation between crystal structure and ordering type we compare the CrB-type HoSi findings with its counterparts (see Table 5).

Simplifying crystalline field point charge calculations [4] (neglecting the conduction electron contributions and with uncertainty concerning the Si charge) showed that the moment direction in CrB-type type compounds is dictated by the predominant second-order crystalline field term V_2^2 that forces the rare earth moments of the 4*c* site with point symmetry *m*2*m* to a direction perpendicular to quantisation axis, i.e. b. This is verified for the R=Tb, Dy and Ho compounds where the magnetic moments are confined to the shortest axis c, while R=Er, Tm moments point along the a-axis (see Table 5) due to a sign change of the Stevens factor α.

On the other hand, the thermal behaviour and the ordering type are by far not uniform in the series as could be expected for isomorphic intermetallic compounds, i.e. R=Tb, Ho, Er compounds are found to have two ordering ranges: the *HT* range with the incommensurate wave vector in two directions $(q_x, 0, q_z)$ and the *LT* the commensurate wave vector (1/2, 0, 1/2). However, Er for an unknown reason was found to have an additional *LT* wave vector. This wave vector occurs in the R=Dy, Tm (0, 0, 1/2) compounds that display only a commensurate type of ordering.

Although the magnetic ordering of HoSi CrB-type resembles that of $TbGe_{0.2}Si_{0.8}$ with respect to the wave vectors their structures differ. HoSi has a uniaxial moment arrangement $||c$ and $TbGe_{0.2}Si_{0.8}$ a planar one within the (0 1 0) plane 20° off the c-axis. This arrangement could be collinear or canted is not distinguishable by powder diffraction.

The FeB-type magnetic ordering of the HoSi compound has been studied for the first time. The T-magnetic phase diagram comprises an *HT* and an *LT* range, described by two symmetry independent wave vectors $(0, q_y, q_z)$ and $(q_x, q_y, 0)$ and a first-order phase transition between them at 16.5 K. The corresponding structures are uniaxial amplitude modulated with the moments along the shortest axis b. The *LT* ordering with the wave vector $(0, q_y, q_z)$ close to the commensurate value $\approx(0, 9/17, 1/11)$ has a T-invariable length. The corresponding structure resembles one of the two *LT* DySi structures, namely that with $\approx(0, 1/2, 1/11)$ (see Table 5). In contrast to the *LT* ordering, the *HT* ordering in HoSi is described by the wave vector $(q_x, q_y, 0)$ close to $\approx(1/11, 8/15, 0)$ that was found to vary with T in such a way that it rotates towards the a-axis within the (0 0 1) plane on heating. The transition between the two phases is of first order with a narrow coexistence range the wave vector jumps to another direction. Whether this occurs via an intermediate structure cannot be answered by the present experiment as explained in previous sections.

A comparison with the behaviour of the isomorphic FeB type members is restricted to the R=Tb, Dy, Ce compounds (Table 5). We note that TmSi of FeB-type does not exist and the neighbouring ErSi has not yet been studied, most likely because it is difficult to stabilise it. From Table 5 one can say that the preferred moment orientation is the shortest axis b. The *R*Si compounds with R=Tb, Dy and Ce have planar structures within the plane (0 0 1) with b as the main axis of antiferromagnetism while HoSi is uniaxial along b. Whether the refined *LT* wave vector of HoSi is incommensurate or commensurate is resolution limited.

The ordering of the FeB-type *R*Si compounds is even more complex than that of the CrB-type. As pointed out in various studies [23–26], this originates from the very low symmetry of the magnetic atoms 4*c* in the *Pnma* space group with the point group .m. Thus the magnetic moments because they have an Ising like behaviour [23] must lie within or perpendicular to the mirror plane m_y. The angle within the plane (0 1 0) depends on the type of *R* ion. This was found for the canted ferrimagnetic structures ($\boldsymbol{q}=0$) of the NdSi and PrSi compounds with the moments close to the a- or c-axis within the plane (0 1 0), see Table 5.

For the *R*Si compounds with R=Ce, Tb, Dy, Ho the preferred moment direction for all four compounds was found to be close to the shortest axis b in the plane (0 0 1). Furthermore symmetry analysis has shown that under the action of the two-component wave vector $(0, q_y, q_z)$, the 4*c* site in the *Pnma* space group splits into two orbits that could have different values and orientation. This would allow also canted magnetic structures for Tb, Dy and Ce instead of collinear structures within the plane (0 0 1). However, powder neutron data are as a rule insensitive to that.

Table 5
Magnetic properties of *RSi* compounds of CrB- and FeB-type [1] from bulk or single crystal magnetic measurements. Magnetic structures from neutron diffraction. Fi: ferri-, AF: antiferro-magnetic, C: commensurate and IC: incommensurate. θ_P: paramagnetic Curie temperature, T_{ord}: ordering temperature, T_t=transition temperature. and μ_{ord}=magnetic moment. References II follows the table and References I is given in the paper.

Compound	Type	μ_{eff} μ_B (at)	θ_P (K)	T_{ord} (K)	T_t (K)	Magn str.	Moment direction	***q*** wave vector	μ_{ord} μ_B (at)	Ref. II	Ref. I
CeSi	FeB			6.1		C, AF, collinear	$\perp c$, 28°/b	(0, 1/2, 1/16)		[39–47]	[10,11]
PrSi	FeB			54		Fi, canted	$\perp b$ 6°/a	0	2.8(3)	[27]	
NdSi	FeB			46		Fi, canted	$\perp b$ 20°/c	0	2.6(3)	[27]	
SmSi	FeB							Unkonwn			
EuSi	FeB							Unkown			
GdSi	FeB	8.4	−1.63	55		AF		Unknown		[34]	
TbSi	FeB	10.1	−8	57	42	IC, *HT*, AF, collinear	$\perp$ c, 16°/b	≈(0, 1/2, 1/8)	8.4		[6–9]
					36–40	IC, *IT*, AF, collinear	$\perp$ c, 20°/b	(0, 1/2, q_z),(0, 1/2, 0)			
					36	C, *LT* AF, collinear	$\perp$ c, 34°/b	(0, 1/2, 0)			
DySi	FeB			38	23.5	IC, *HT*, AF, collinear	$\perp$ c	(0, q_y, q_z) ≈ (0, 1/2, 1/7)		[36,37]	[12–14]
						C, IC, *LT* AF, collin.	$\perp c$ 2°/b; 22°/b	(0, 1/2, 1/6);(0, q_y, q_z) ≈ (0, 1/2, 1/11)			
HoSi	FeB	–	–	25	16.5	IC *HT* AF, uniaxial	$\|\|b$	(q_x, q_y, 0) ≈ (1/11, 1/2, 0)		This paper	[5,6]
						IC *LT* AF, uniaxial	$\|\|b$	(0, q_y, q_z) ≈ (0, 1/2, 1/11)			
ErSi	FeB	–	–					Unknown	–		
$TbGe_{0.2}Si_{0.8}$	CrB	9.58	12	58	45.5	IC *HT* AF, collinear	$\perp b$, 20°/c	(q_x, 0, q_z)	8.4	[28–31]	[3,4]
						C, *LT* AF, collinear	$\perp b$	(1/2, 0, 1/2)			
$DyGe_{0.2}Si_{0.8}$	CrB		16	43		C, AF, uniaxial	$\|\|c$	(0, 0, 1/2)	8.8	[35]	[4]
	CrB			39		C, AF, uniaxial	$\|\|c$				[14]
DySi					23.5	C, AF, uniaxial	Monoclinic,dist.	(0, 0, 1/2)			
HoSi	CrB	10.77	2	25		IC, *HT*, AF, uniaxial	$\|\|c$	(q_z, 0, q_z)		This paper	[4–6]
					16.5	AF, *LT*, AF, uniaxial	$\|\|c$	(1/2, 0, 1/2)			
ErSi	CrB	9.38	−5	11.5		IC, *HT*, AF, uniaxial	$\|\|a$	(q_z, 0, q_z)	8.3	[28,31–33]	
					7.25	C, *LT*, AF, uniaxial		(1/2, 0, 1/2)(0, 1/2, 0)			
TmSi	CrB	7.45	10	10		C, AF, uniaxial	$\|\|a$	(0, 0, 1/2)	5.0		[3,4]
YbSi	CrB			1.6		AF		Unknown	0.2–0.3	[38]	

Amplitude modulated phases are very common in rare earth intermetallics and the *R*Si compounds present further examples. Usually the amplitude modulated phases appear below the Neel temperature and undergo transitions to equal moment structures (commensurate lock-in phases or antiphase domain structures when higher harmonics appear) at low temperatures for entropy reasons. Their existence arises most likely from the competition between the long-range oscillatory nature of the exchange interaction between the localised 4*f* moments, the crystal field anisotropy and small quadrupolar interionic interactions [2] The exchange interaction is of the RKKK type in rare earth compounds. It is an indirect interaction mediated mainly by the polarisation of the 5*d* electrons residing in narrow conduction bands, the very small radial extent of the 4*f* rare electrons not allowing direct interactions. Apparently the large variety of observed structures arises from the low symmetry site of the rare earth at the corners of elongated trigonal prism in both CrB and FeB type modifications that most likely relate to the predominant role of crystalline field effects that may introduce important anisotropy and define the moment orientation. While it is obvious that the crystal field anisotropy has a distinct influence of on the moment *direction* in the *R*Si compounds [4]; the influence of the crystal field anisotropy on the *type* of ordering (***q*** vector) is less evident. Probably this influence is comparatively small in the *R*Si compounds. Prominent examples (see Table 5) that would justify this conclusion are the magnetic structures in FeB type HoSi where the incommensurate structures change with temperature from (q_x, q_y, 0) to (0, q_y, q_z) even though the moment direction does not change and remains parallel to the *b* direction, or the incommensurate structures (q_x, 0, q_z) both present in CrB type HoSi and in CrB type ErSi although the moment direction is along different directions in both compounds.

Appendix

To facilitate reading we summarise in Table 5 the presently available information and the references concerning the magnetic properties and structures of the *R*Si compounds. The reference numbers [27–47] given in column Ref. II regard exclusively the review table. These references were not discussed in the main part of the paper. The reference numbers in column Ref. I are those of the reference list of the paper. We recall that the more recent review on *R*Si compounds dates over 10 years [2].

References I

[1] D. Hohnke, E. Parthé, Acta Cryst 20 (1966) 572.
[2] D. Gignoux, D. Schmitt, in: K.H.J. Buschow (Ed.), Handbook of Magnetic Materials, vol. 10, Elsevier, Amsterdam, 1997, p. 239.
[3] V.N. Nguyen, A. Barlet, J. Laforest, J. Phys. Coll. C1 32 (Suppl. no. 2–3) (1971) C1–1133.
[4] V.N. Nguyen, J. Rossat-Mignod, F. Tcheou, Solid State Commun. 17 (1975).
[5] P. Schobinger-Papamantellos, K.H.J. Buschow, J. Solid State Chem. 70 (1987) 249.
[6] P. Schobinger-Papamantellos, K.H.J. Buschow, T. Janssen, EPDIC-3 Third European Powder Diffraction Conference, Vienna, Austria, Sept. 25–28, 1993. Materials Science Forum, vol. 166–169, 1994, 479.
[7] P. Schobinger-Papamantellos, K.H.J. Buschow, F. Maaroufi, P. Toledano, J. Phys. Coll. C8 49 (Suppl. no. 12) (1988) C8–423.
[8] P. Schobinger-Papamantellos, T. Janssen, K.H.J. Buschow, J. Magn. Magn. Mater. 127 (1993) 115.
[9] V.N. Nguyen, J. Laforest, J. Sivardiere, Solid State Commun 8 (1970) 23.
[10] P. Schobinger-Papamantellos, K.H.J. Buschow, J. Magn. Magn. Mater. 130 (1994) 242–246.
[11] P. Schobinger-Papamantellos, M. Kenzelmann, A. Schenck, F.N. Gygax, K.H.J. Buschow, C. Ritter, Physica B 349 (2004) 100.
[12] P. Schobinger-Papamantellos, K.H.J. Buschow, J. Rodríguez-Carvajal, C. Ritter, J. Magn. Magn. Mater. 321 (2009) 2842.
[13] P. Schobinger-Papamantellos, J. Rodríguez-Carvajal, K.H.J. Buschow, C. Ritter, J. Magn. Magn. Mater. 322 (2010) 119–131.
[14] P. Schobinger-Papamantellos, M. Brunelli, J. Rodríguez-Carvajal, K.H.J. Buschow, C. Ritter, F. Gramm, J. Magn. Magn. Mater. 323 (2011) 903.
[15] J. Rodríguez-Carvajal. Physica B 192 (1993) 55. The programs of the FullProf Suite and their corresponding documentation can be obtained from the Web at 〈http://www.ill.eu/sites/fullprof/〉.
[16] L.C. Chapon, J. Rodríguez-Carvajal, (unpublished). FullProf Studio is a program of the FullProf Suite that is freely available in the site given in [15].
[17] J. Roger, V. Babizhetskyy, T. Guizouarn, K. Hiebl, R. Guérin, J.-F. Halet, J. Alloys Compd. 417 (2006) 72.
[18] J. Rossat-Mignod, Methods of Experimental Physics: Neutron Scattering, vol. 3, Academic Press, New York, 1987.
[19] R.B. von Dreele, J. Rodriguez-Carvajal, Intensity of a Bragg reflection, section 3.3.4.4: limitations of neutron scattering for determining magnetic structures, in: R.E. Dinnebier, S.J.L. Billinge (Eds.), Powder Diffraction, RSC Publishing, ISBN 978-0-85404-231-9, 2008 (Chapter 3).
[20] G. Shirane, Acta Crystallogr. 12 (1959) 282.
[21] J. Rodríguez-Carvajal, Program Moment, Unpublished.
[22] A. Raman, H. Steinfink, Acta Crystallogr 22 (1967) 688.
[23] J. Rossat-Mignod, F. Tscheou, J. de Phys. 33 (1972) 423.
[24] R. Iraldi, V.N. Nguyen, J. Rossat-Mignodt, F. Tcheou, Solid State Commun. 15 (1974) 1543.
[25] J. Rossat-Mignod, J. de Phys. Coll. C5 40 (suppl. no. 5) (1979) C5–95.
[26] D. Gignoux, D. Schmitt, J. de Phys. 35 (1974) 455.

References II

[27] V.N. Nguyen, F. Tcheou, J. Rossat-Mignod, Solid State Commun 23 (1977) 821.
[28] V.N. Nguyen, F. Tcheou, J. Rossat-Mignod, J. Phys 45 (1984) 163.
[29] P. Schobinger-Papamantellos, K.H.J. Buschow, J. Magn. Magn. Mater 62 (1986) 15.
[30] P. Schobinger-Papamantellos, K.H.J. Buschow, J. Magn. Magn. Mater. 71 (1988) 134.
[31] V.N. Nguyen, J. Sivardiere, A. Apostolov, Colloques Internationaux du CNRS Les Elements des Terres Rares, Grenoble, Vol. 2, CNRS, Paris–Grenoble, 1970, p. 261.
[32] P. Thuéry, F. El Maziani, M. Clin, P. Schobinger-Papamantellos, K.H.J. Buschow, J. Magn. Magn. Mater. 127 (1993) 93.
[33] P. Thuéry, G. André, F. Maziani, M. Clin, P. Schobinger-Papamantellos, J. Magn. Magn. Mater 109 (1992) 197–208.
[34] L.D. Tung, M.R. Lees, G. Balakrishnan, D.McK. Paul, P. Schobinger-Papamantellos, O. Tegus, P.E. Brommer, K.H.J. Buschow, Phys. Rev. B 71 (2005) 144410.
[35] V.N. Nguyen, J. Rossat-Mignod, F. Tcheou, J. Phys. Proc. Int. Conf. Magn., vol. III 22–28 August 1973 Nauka, Moscow, 1974, s185.
[36] R. Iraldi, V.N. Nguyen, J. Rossat-Mignodt, F. Tcheou, Solid State Commun. 15 (1974) 1543.
[37] R. Nirmala, A.V. Morozkin, D. Buddhikot, A.K. Nigam, J. Magn. Magn. Mater. 320 (2008) 1184.
[38] P. Bonville, F. Gonzalez-Jimenez, P.D. Jaccard, G. Jehanno, J. Phys.—Condens. Matter 1 (44) (1989) 8567.
[39] S.A. Shaheen, Phys. Rev. B 36 (1987) 5472. CeSi Observation Of The Highest Ground-State Magnetic-Moment Of Ce In Cesi - Possibility Of A Quartet Ground-State.
[40] S.A. Shaheen, J. Appl. Phys. 63 (1988) 3411 Part 2.
[41] S. Noguchi, K. Okuda, H. Nojiri, et al., J. Magn. Magn. Mater 177 (1998) 403.
[42] K. Mimura, T. Takase, H. Mizohata, et al., J. Electron Spectrosc. Relat. Phenom. 114 (2001) 723.
[43] S. Noguchi, Phys. B—Condens. Matter 329 (2003) 491.
[44] S. Noguchi, S. Miyagawa, H.A. Katori, et al., J. Magn. Magn. Mater. 272 (2004) E1533.
[45] K. Mimura, Y. Watanabe, H. Mizohata, et al., Phys. B—Condens. Matter 351 (2004) 295.
[46] K. Mimura, S. Noguchi, M. Suzuki, et al., J. Electron Spectrosc. Relat. Phenom. 144 (2005) 715.
[47] M. Münzenberg, W. Felsch, P. Schaaf, Phys. Rev. B 76 (2007) 014427.